Structure and transport properties of LiTFSI-based deep eutectic electrolytes from machine learning interatomic potential simulations

Omid Shayestehpour[a)] and Stefan Zahn
Leibniz Institute of Surface Engineering, 04318 Leipzig, Germany

(Dated: 8 August 2024)

Deep Eutectic Solvents have recently gained significant attention as versatile and inexpensive materials with many desirable properties and a wide range of applications. In particular, their similar characteristics to ionic liquids, make them a promising class of liquid electrolytes for electrochemical applications. In this study, we utilized a local equivariant neural network interatomic potential model to study a series of deep eutectic electrolytes based on lithium bis(trifluoromethanesulfonyl)imide (LiTFSI) by molecular dynamics (MD) simulations. The use of equivariant features combined with the strict locality result in highly accurate, data-efficient and scalable interatomic potentials enabling large-scale MD simulations of these liquids with first-principles accuracy. Comparing the structure of the liquids to reported results from classical force field (FF) simulations indicates that ion–ion interactions are not accurately characterized by FFs. Furthermore, close contacts between lithium ions bridged by oxygen atoms of two amide molecules are observed. The computed cationic transport numbers (t^+) and the estimated ratios of Li$^+$–amide lifetime ($\tau_{\text{Li–amide}}$) to the amide's rotational relaxation time (τ_R), combined with the ionic conductivity trend, suggest a more structural Li$^+$ transport mechanism in the LiTFSI:urea mixture through exchange of amide molecules. However, a vehicular transport could have a larger contribution to Li$^+$ ion transport in the LiTFSI:N-methylacetamide electrolyte. Moreover, comparable diffusivities of Li$^+$ cation and TFSI$^-$ anion and a $\tau_{\text{Li–amide}}/\tau_\text{R}$ close to unity, indicate that vehicular and solvent-exchange mechanisms have rather equal contributions to Li$^+$ ion transport in the LiTFSI:acetamide system.

I. INTRODUCTION

Deep eutectic solvents (DESs) are a class of liquid mixtures with a melting point considerably lower than that of their individual components, and commonly even lower than the predicted ideal eutectic point[1–3]. DESs share many of the desirable properties of ionic liquids (ILs), such as low vapor pressure, thermal and chemical stability, and tunable properties[4,5]. Moreover, they possess several advantages over conventional ILs, including facile synthesis, lower production costs, generally lower toxicity, and higher ionic conductivities, which make them a promising class of materials for electrochemical applications[6–8]. Deep eutectic electrolytes (DEEs) refer to those DESs applicable as electrolytes in electrochemical devices such as redox flow batteries[9–11] and lithium-ion batteries (LIBs)[12–14]. DEEs are typically binary mixtures consisting of a metal salt, like lithium bis(trifluoromethanesulfonyl)imide (LiTFSI), and an organic hydrogen bond donor, such as an amide[15–17].

Synthesizing novel DEEs with desirable properties from a large number of potential components remains a challenging task, which demands a detailed understanding of the interactions among different components at the molecular scale and the diffusion behavior of ionic species. Computer simulations are effective and valuable tools in this regard, providing insights into the nature of atomic-scale interactions and ion transport mechanisms in liquid electrolytes. There are several molecular dynamics (MD) simulation studies of eutectic electrolytes, with the majority of them based on classical force fields (FFs)[13,18–20] and many-body polarizable FF models[21–24]. The length and time-scales accessible by FF simulations make them particularly suitable for MD simulations of molecular ionic liquids, which typically have slow dynamics, and require sufficiently large system sizes and long simulation times to converge structural and, especially, dynamical properties[25]. However, the accuracy of FF models is limited by the underlying functions describing the atomic interactions and the quality of their parameterization. It is well-known that two-body FF models based on fixed atomic charges significantly underestimate the dynamics and diffusion properties of molecular ionic liquids, mainly due to the lack of polarization effects involving the ionic species[26–28]. While polarizable many-body FFs greatly improve the dynamics of these liquids, showing much better agreement with experiments, they require careful validation and refinement against costly first-principles molecular dynamics (FPMD) simulations and experiments, and generally lack transferability[23,29,30].

In recent years, machine-learned interatomic potentials (MLIPs) have enabled computationally efficient MD simulations of complex materials and chemical processes with the accuracy of first-principles methods[31–34]. In particular, MLIP-based MD simulations of ILs and DESs have been already reported in the literature[35–40]. A range of MLIPs has been introduced in recent years, including linear and kernel-based models[41–44], Gaussian approximation[45,46], and neural network interatomic potentials (NNIPs)[47–54]. While NNIPs, commonly based on invariant descriptors of the local atomic environment, can successfully scale to extremely large system sizes, they typically require large training sets of reference electronic structure calculations to achieve reasonable accuracy[38]. More recently, NNIP architectures based on equivariant representations, and atom-centered message-passing neural networks (MPNNs) have shown remarkable accuracy and data-

---

[a)] Electronic mail: omid.shayestehpour@uni-leipzig.de efficiency[55–58]. However, their iterative information propagation beyond the local atomic environment leads to large receptive fields with many effective neighbors for each atom, which hinders parallel computation and limits the length-scales accessible by these models[59,60]. There have been some efforts to reduce the computational complexity of equivariant MPNN models and enable more efficient implementation and large-scale simulations, including strictly local representation of atom environments[59] and incorporation of a runtime geometry calculation strategy combined with the use of inner product in place of computationally expensive Clebsch–Gordan tensor product[61].

In this work, we utilized the Allegro model[59], a strictly local equivariant NNIP architecture, to study a series of LiTFSI-based DEEs by MD simulations. The use of equivariant representations, combined with the strict locality, result in highly accurate, data-efficient and scalable interatomic potentials enabling large-scale MD simulations of these DEEs with the target density-functional theory (DFT) accuracy. We have trained a set of NNIPs on datasets constructed using short DFT-based FPMD simulations and a number of selected structures using an iterative active learning scheme based on calibrated ensemble uncertainties. The studied systems comprise mixtures of LiTFSI (T_m = 234 °C) with: (1) urea (T_m = 132.7 °C) in 1:3.5 molar ratio with a reported melting point of −37.6 °C[15], which we refer to as URA; (2) acetamide (T_m = 81.2 °C) in 1:4 molar ratio with a reported melting point of −67 °C[16], which we refer to as ACT; and (3) N-methylacetamide (T_m = 28 °C) in 1:4 molar ratio with a reported melting point of −72 °C[17], which we refer to as NMA. The selected molar ratios are the reported eutectic compositions for these DEEs. The aim of this study is to evaluate the ability of equivariant MLIPs to accurately represent the potential energy surface (PES) of eutectic electrolytes in a data-efficient manner, and further investigate the role of the amide in the structuring of the liquid, melting point depression, ion diffusion, ionic conductivity, and ion transport mechanisms in LiTFSI-based DEEs.

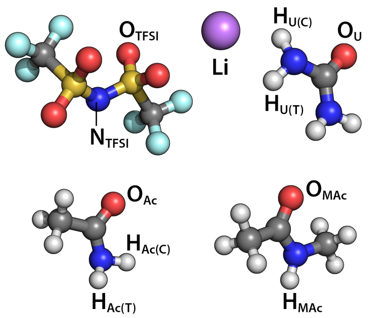

FIG. 1. Chemical structures of lithium (Li) bis(trifluoromethanesulfonyl)imide (TFSI) (top left), urea (U) (top right), acetamide (Ac) (bottom left), and N-methylacetamide (MAc) (bottom right) with the corresponding atom labels used throughout this study. Atom color scheme: white: H, gray: C, blue: N, red: O, cyan: F, yellow: S, purple: Li.

II. METHODS

A. Neural Network Interatomic Potential Model

We utilized Allegro[59], an equivariant NNIP, which uses strictly local many-body equivariant representations to map the atomic coordinates to the corresponding potential energy and atomic forces. In the Allegro model, the total energy of a system, E, is decomposed into per-atom energies E_i,

$$E = \sum_{i}^{N} \sigma_{Z_i} E_i + \mu_{Z_i} \tag{1}$$

with σ_{Z_i} and μ_{Z_i} as per-species scale and shift parameters. The per-atom energy E_i further decomposed into a sum of pairwise energies E_{ij},

$$E_i = \sum_{j \in \mathcal{N}(i)} \sigma_{Z_i, Z_j} E_{ij} \tag{2}$$

where j runs over neighbors of the central atom i within a selected cutoff radius, and σ_{Z_i, Z_j} is a per-species-pair scaling factor. It is important to note that the pairwise energies E_{ij}, depend on all neighboring atoms k in the local environment of atom i, and that they are assigned to ordered pairs of neighboring atoms. The latter means that E_{ij} and E_{ji} contribute to different per-atom energies E_i and E_j, respectively, and that $E_{ij} \neq E_{ji}$. This results in the strict locality of the Allegro model, as per-atom energies depend only on the environments of the corresponding central atoms within the selected cutoff radius.

The Allegro model learns representations associated with ordered pairs of neighboring atoms using invariant scalar features, and equivariant features consisting of higher rank tensors. The scalar features, $\boldsymbol{X}^{ij,L=0}$, are initialized by one-hot encoding of the center and neighbor atom species Z_i and Z_j, and the projection of the interatomic distance r_{ij} onto a radial basis using the two-body latent multi-layer perceptron (MLP). The initial equivariant features, $\boldsymbol{V}^{ij,L=0}_{n,\ell,p}$, are constructed as a linear embedding of the spherical harmonic projection of the unit displacement vector $\boldsymbol{r}_{ij} = \boldsymbol{r}_j - \boldsymbol{r}_i$:

$$\boldsymbol{V}^{ij,L=0}_{n,\ell,p} = W^{ij,L=0}_{n,\ell,p} \boldsymbol{Y}^{ij}_{\ell,p}, \tag{3}$$

where the scalar weights, $W^{ij,L=0}_{n,\ell,p}$, for each center-neighbor pair ij are output of the embedding MLP acting on the initial two-body scalar features. The two types of features interact with each other at each layer of the network, using the latent MLP, and the final pair energy E_{ij} is the output of an MLP acting on the final layer's scalar features. Finally, the force on atom i, $\boldsymbol{F}_i$, is computed as the negative gradient of the total energy with respect to the position of atom i, which results in an energy-conserving force field,

$$\boldsymbol{F}_i = -\nabla_i E. \tag{4}$$

The model is trained using a joint mean squared error (MSE) loss function of per-atom energies and forces:

$$\mathcal{L} = \lambda_E \left(\frac{\hat{E} - E}{N} \right)^2 + \frac{\lambda_F}{3N} \sum_{i}^{N} \sum_{\alpha \in x,y,z} \|\hat{F}_{i,\alpha} - F_{i,\alpha}\|^2 \quad (5)$$

where N is the number of atoms, E and $F_{i,\alpha}$ are total energy and the force component on atom i in direction α, respectively. λ_E, λ_F are weights of the per-atom energy and force terms, respectively.

As model hyperparameters, we use two interaction layers, features of even and odd parity and maximal rotation order $\ell_{max} = 2$ in spherical harmonics embedding. Through hyperparameter tests, we found these values to be a good trade-off between computational cost and accuracy. The two-body latent MLP has 4 hidden layers of dimensions [32, 64, 128, 256], and the latent MLP consist of 3 hidden layers of dimensions [256, 256, 256], both using SiLU activation functions. The embedding MLP is a single matrix multiplication without a hidden layer and nonlinearity. The final pair energy MLP has one hidden layer of dimension 128 and no nonlinearity. All MLPs were initialized using a uniform distribution with unit variance. We used a radial cutoff of 6.0 Å and a basis of 8 trainable Bessel functions for the radial basis encoding with the polynomial envelope function using $p = 6$. The models were trained by minimizing the joint loss in Eq. 5 using a weighting of 1 for both the per-atom energy and the force term. We used the Adam optimizer[62], with default parameters, a learning rate of 0.001 and a batch size of 1. The models were trained for a maximum of 200 epochs with an average training time of 1 day. We observed that more training epochs, despite small improvements of validation errors, has a negative impact on generalization capabilities of the models and results in less stable simulations. The MLIPs were trained using the Allegro code version 0.2.0, with the NequIP code version 0.6.0[56], e3nn code version 0.5.1[63], and PyTorch version 1.11.0[64]. All models were trained with `float32` precision on a single NVIDIA A100 graphics processing unit (GPU).

B. Reference Datasets and Active Learning

The primary reference datasets are constructed based on a set of short (20 ps) FPMD trajectories. The FPMD simulations were performed for mixtures of 8 LiTFSI ion pairs with: 28 urea molecules in the URA system; 32 acetamide molecules in the ACT system; and 32 N-methylacetamide molecules in the NMA system using the CP2K package[65]. Details of the FPMD simulations are provided in the supporting materials. For each system, a total number of 4500 structures, from the first 15 ps of the trajectories, were selected for model training and validation. The structures are sampled with an increasing time-lag between successive frames. The remaining 5 ps of the trajectories were used to construct test sets each containing 500 structures.

Additionally, we employed an active learning (AL) scheme based on computed uncertainties from an ensemble of the trained models to extend the primary datasets. As a measure of uncertainty, we used the standard deviation of the predicted atomic forces. In contrast to energies, forces determine the dynamics of the system and typically show higher variability outside the training domain. The uncertainty, u, is defined as the square root of the mean of component-wise variances of the predicted forces,

$$u = \sqrt{\frac{1}{3N_c} \sum_{i}^{N_c} \sum_{\alpha \in x,y,z} \left(\hat{F}_{i,\alpha} - \bar{F}_{\alpha} \right)^2}, \quad (6)$$

where N_c is the number of constituent models (we used $N_c = 3$), $\hat{F}_{i,\alpha}$ denotes the α-component of model i's predicted force, and $\bar{F}_{\alpha}$ denotes the mean of the α-component of the predicted forces of all constituent models. The models of each ensemble are trained with different initialization of NNs weights and different training/validation splits of the dataset.

Many heuristic uncertainty metrics, such as the ensemble-based uncertainty quantification (UQ), assume that the model errors have a Gaussian distribution. The reliance on the assumption of normally distributed errors is a weakness of ensemble-base uncertainties, since the error types encountered in MLIPs are generally not normally distributed[66,67]. As a result, the ensemble uncertainties are typically not well calibrated and often underestimate actual errors. Specifically, poor calibration complicates defining an appropriate uncertainty threshold for selection of high-error structures in AL[68,69]. To address this issue, we utilize conformal prediction (CP), a distribution-free UQ method, which computes a re-scaling factor based on predicted uncertainties and prediction errors on a calibration set[67,70]. In the CP method, the confidence level $(1 - \alpha)$ is defined such that the probability of underestimating the actual error, on configurations drawn from the same distribution as the calibration set, is at most α. Thus, CP can convert a heuristic notion of uncertainty (u) to a statistically rigorous and calibrated one, and help align atomic force errors with their corresponding uncertainty values (Fig. 2).

In our iterative AL scheme, the configurational space of each system is explored by MLIP-based MD simulations. In each AL iteration, we performed 10 separate MD simulations, for each of the systems, starting from different initial structures. MD simulations were performed in LAMMPS[71], with the `pair_allegro` extension[59], using NVT ensemble (400 K) and a 0.5 fs timestep for 50–100 ps. The atomic configurations were uniformly sampled at each 100 timesteps, and a small subset of those configurations, sized N_{calib}, selected as a calibration set. Subsequently, the structures in the calibration set were labeled with the reference DFT forces and the corresponding prediction errors are computed as $\Delta \boldsymbol{F}_i = 1/3 \sum_{\alpha} \|F_{i,\alpha} - \bar{F}_{i,\alpha}\|$, where $F_{i,\alpha}$ and $\bar{F}_{i,\alpha}$ are the true and ensemble-mean predicted force on atom i in direction $\alpha \in x, y, z$, respectively. We used the CP method from the `AmpTorch` package[72] to perform quantile regression with chosen hyperparameter $\alpha = 0.1$ (i.e. 90% confidence) on the calibration data to compute the $(1 - \alpha)(N_{calib} + 1)/N_{calib}$-th quantile denoted as $\hat{q}$. Then

$\hat{q}$ value is applied to the remaining of sampled atomic configurations to compute their calibrated uncertainties $\tilde{u} = u \cdot \hat{q}$. Finally, a set of structures with a maximal atomic force uncertainty above a certain threshold ($\tilde{u} \geq 3\,\mathrm{kcal\,mol^{-1}\,Å^{-1}}$) are selected to be labeled with the reference DFT energies and atomic forces to extend the dataset. Additionally, the selected atomic structures were inspected using the molecule recognition tool of the TRAVIS package[73] to screen out possible unphysical atomic configurations prior to the DFT calculations. We performed the iterative AL cycles, consisting of model training, exploration, selection and labeling, until the number of high-uncertainty structures in the selection step were less than 50. Interestingly, only two AL cycles were required to fulfill our set objective and achieve highly-accurate and robust MLIPs. This result is in sharp contrast to our previous observations for MLIPs based on invariant features, which required minimum ten AL iterations to achieve sufficiently-long and stable simulations[38]. This, as has been shown before[56,58,60], is the direct result of the inclusion of equivariant features in the representation of the atomic environments, which enables much more data-efficient learning compared to invariant models. At the end of our AL cycles we collected a total number of 880 data points for the URA system, and 720 data points for each of the ACT and the NMA systems.

C. Molecular Dynamics Simulations

MD simulations were carried out with LAMMPS[71], using the `pair_allegro` extension[59]. We used a canonical (NVT) ensemble at 353 K (80 °C) with an integrator timestep of 0.5 fs, and atom positions and velocities were collected each 10 fs. A Nosé–Hoover chain thermostat was used with a relaxation time of 0.05 ps[74]. Mixtures of 128 LiTFSI ion pairs with: 448 urea molecules for the URA system (1:3.5 molar ratio); 512 acetamide molecules for the ACT system (1:4 molar ratio); and 512 N-methylacetamide molecules for the NMA system (1:4 molar ratio) were simulated in a periodic cubic box of size 40.3 Å, 43.3 Å and 46.1 Å, respectively. MD simulations are started from well-equilibrated structures taken from classical MD simulations using the general AMBER FF[75–77]. The systems were simulated for 200 ps followed by production runs of 3 ns for the URA system and 2 ns for the ACT and NMA systems. The reported results are computed from the average of three separate MD simulations for each of the studied systems starting from different initial configurations. The energy drifts during the MD simulations were approximately $0.002\,\mathrm{kcal\,mol^{-1}\,atom^{-1}}$ over the course of 1 ns, indicating that the energies are very well conserved during the simulations. MD simulation were performed on 8 NVIDIA A30 GPUs with an average performance of 0.65 ns/day. All distribution functions, mean-square displacements, rotational relaxation times, and pair lifetimes were computed using the TRAVIS package[73,78].

III. RESULTS AND DISCUSSION

A. Model Accuracy

The accuracy of the trained MLIPs was evaluated on test sets of 500 atomic configurations. Fig. 3 shows the error distributions of the predicted values for per-atom energy and atomic force compared to the reference DFT values. The mean absolute errors (MAEs) of predicted per-atom energies are in the range of $0.003–0.009\,\mathrm{kcal\,mol^{-1}}$, indicating that our MLIPs can predict the energy of the structures with a great accuracy. More importantly, the root mean squared errors (RMSEs) of atomic forces from all three models are bellow $1\,\mathrm{kcal\,mol^{-1}\,Å^{-1}}$. These results demonstrate the remarkable generalization capabilities of MLIPs based on equivariant representations compared to invariant models, which typically require tens of thousands of data points and many AL iterations to achieve comparable accuracy[38,39]. In Fig. S2 of the supplementary material, the error distributions of the atomic forces for each of the chemical species, and the corresponding RMSEs, indicate that the prediction errors are not uniform among different chemical elements. The lighter hydrogen and lithium atoms have smaller predicted force errors, while sulfur and carbon atoms show larger errors than average. It is worth mentioning that through our model training experiments, we found that inclusion of highly correlated atomic configurations in the training set is crucial to accurately predict atomic forces on some of the chemical species. The source of this dependence is not yet clear to us and remains the subject of future investigations.

To further investigate the fidelity of the MLIPs, we compared the liquid structures from MLIP-based MD simulations to the reference FPMD simulations using radial distribution functions. The MD simulations were performed on systems of the same size as the DFT-based simulations. The selected radial distribution functions in Fig. 4 show excellent agreement between MLIP-based and DFT simulations. Additionally, the dynamics of the systems at short timescales were compared to the reference FPMD simulations via velocity autocorrelation functions. The center-of-mass (CoM) velocity autocorrelation functions of the $\mathrm{Li^+}$ cation, $\mathrm{TFSI^-}$ anion, and amide molecule, as shown in Fig. S1 of the supplementary material, perfectly match the results from the FPMD simulations.

B. Structure of the Liquids

The liquid structure of the studied DEEs are investigated by radial distribution functions (RDFs), $g_{\alpha\beta}(r)$, which denote the ratio of the local number density of species β around α to the total number density of β. Accordingly, the coordination number, $N_{\alpha\beta}(r_c)$, of β species around α can be obtained as

$$N_{\alpha\beta}(r_c) = \rho_\beta \int_0^{r_c} 4\pi r^2 g_{\alpha\beta}(r)dr, \tag{7}$$

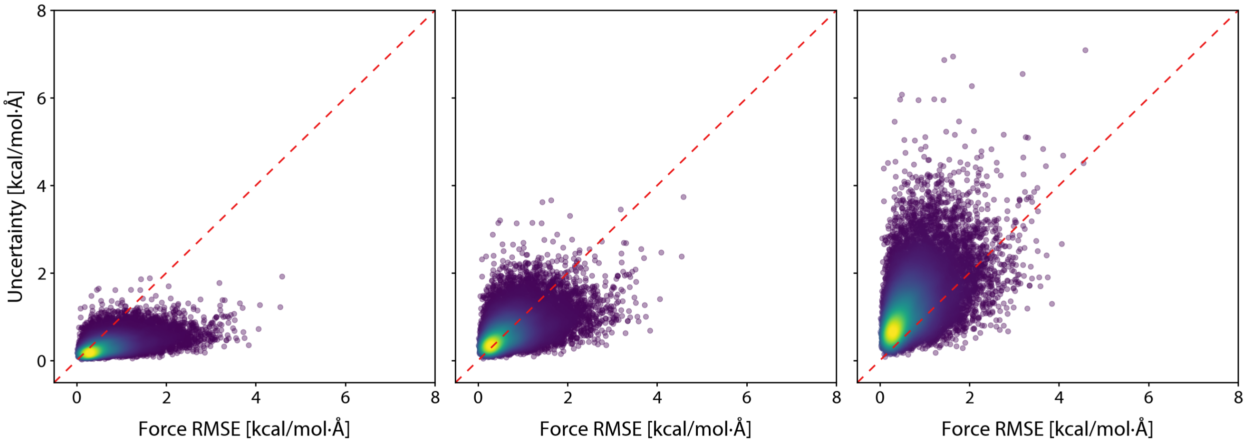

FIG. 2. Correlation of atomic force uncertainties with atomic force RMSE for 50 test structures. The left panel shows the heuristic uncertainties (u), while middle and right panels show calibrated uncertainties ($\tilde{u}$) using CP method with 60% and 90% confidence level, respectively. The color maps (from purple to yellow) denote density in close proximity using kernel density estimate (KDE) analysis. The brighter colors denote the more densely populated regions. Calibrating uncertainties with a high confidence level helps align the large actual errors with the corresponding uncertainty, shifting the points to or above the red diagonal line.

where r_c denotes an arbitrarily chosen distance. In Fig. 5, the strong RDF peaks of Li–O_{TFSI} and Li–O_{amide} indicate that lithium cations are strongly coordinated by the oxygen atoms from both the $TFSI^-$ anions and the carbonyl group of the amide molecules. However, the RDF peaks of oxygen atoms of the amide molecules around Li^+ ion have notably higher intensity compared to those of the $TFSI^-$ oxygen atoms, and the coordination numbers in Table I also show that significantly more amide oxygen atoms coordinate with the lithium cation. This preferred interaction can be attributed to the negative partial charge on oxygen atoms of amides due to their resonance structure, and the high dipole moment of these molecules, which favors the oxygen orientation towards lithium ions[15]. On average, 3.25 O_U atoms can be found around Li^+ cations in the URA mixture, which slightly increases to 3.48 and 3.47 for O_{Ac} and O_{MAc} in the ACT and NMA mixtures, respectively. Please note, more amide molecules are available per Li^+ ion in these two mixtures. Interestingly, the total number of oxygen atoms coordinating with a lithium cation is approximately four for all three DEEs. This aligns with FF simulation results for the URA system[19], but contradicts the reported value (of about 5.6) for the ACT system[18].

The RDF plots of the oxygen atoms (O_{TFSI} and O_{amide}), as hydrogen bond acceptors, around hydrogen atoms of the amine groups in Fig. 6, and the corresponding coordination numbers in Table I, indicate that hydrogen bonding may also play a role in the structuring of these liquids. On average, one oxygen atom can be found in the first coordination shell of the amino hydrogen atoms of amide molecules. Furthermore, for the primary amine groups of urea and acetamide, the RDF plots, in Fig. S3 of the supplementary material, reveal that there is a preferred interaction between $O_{U/Ac}$ atoms and hydrogen atoms in *cis* position of the carbonyl group ($H_{U(C)}$ and $H_{Ac(C)}$), while O_{TFSI} atoms preferably interact with the hydrogen atoms in *trans* position ($H_{U(T)}$ and $H_{Ac(T)}$). This effect is also visible in the spatial distribution plots of Fig. 10 (d and e), in which a notably larger density cloud of $TFSI^-$ ion could be found close to the hydrogen atoms in *trans* position compared to those in *cis* position, while the opposite can be observed for the density cloud of amide. A similar finding has been observed in our simulation studies of choline chloride–urea DES, which was attributed to the possible formation of double hydrogen bonds between two urea (or acetamide) molecules via *cis* hydrogen atoms[38]. Additionally, in our simulations, specific arrangements of urea or acetamide molecules around a lithium ion could be observed that also enable a close contact of an amide's oxygen to a *cis* hydrogen atom of a neighboring amide molecule (see Fig. 8a and c). These results indicate that the strong interactions between the oxygen atom of amide molecules and the lithium cation effectively disrupt both the hydrogen-bond network in pure amide, and the crystal lattice of the LiTFSI salt by replacing the anion in the first coordination shell of a Li^+ cation, while enabling weaker anion–amide interaction via hydrogen bonding[13,15,79]. This is in contrast to most common DESs, such as mixtures of choline chloride, in which the formation of hydrogen bonds between the anion and amide molecules is the main driving force for the deep eutectic behavior[80].

To characterize the liquid structures at the molecular level, the CoM RDFs for the three DEEs are compared in Fig. 7. The Li–amide RDFs are similar in all three mixtures, with a small shift of the main peak's position in the NMA system caused by the change in center of mass of the N-methylacetamide molecule compared to urea and acetamide. The first coordination shells in Li–TFSI RDFs from 2.6 to 5.2 Å show a hint of a double peak structure, which can be assigned to monodentate and bidentate coordinating $TFSI^-$ ions[81,82]. The first peak re-

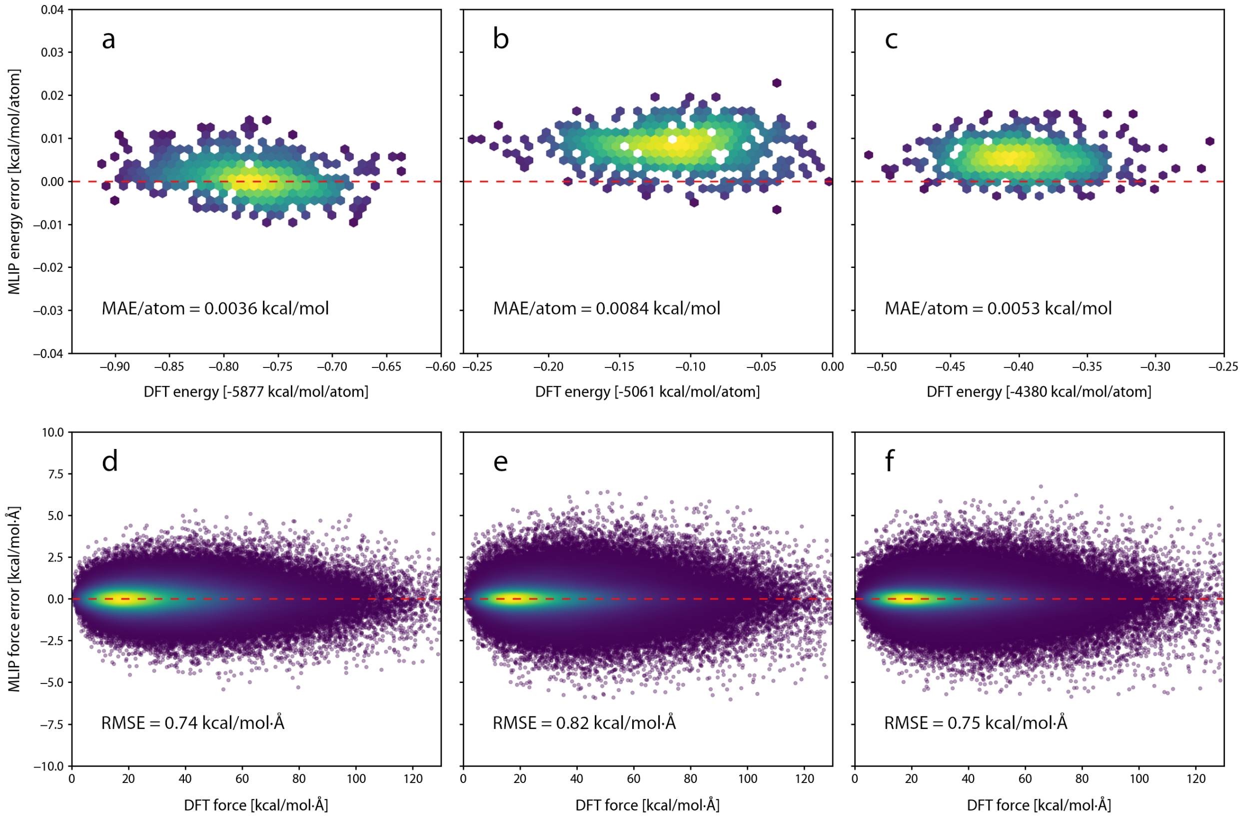

FIG. 3. Error distribution plots with kernel density estimate (KDE) as color maps, showing MLIPs prediction errors on 500 test structures. Top panel shows hexbin histograms of per-atom energy errors for the URA (a), ACT (b) and NMA (c) system. Bottom panel shows atomic force errors for the URA (d), ACT (e) and NMA (f) system. The color maps (from purple to yellow) show the points density in close proximity. The brighter colors denote the more densely populated regions.

TABLE I. Coordination number, $N_{\alpha\beta}(r_c)$, of oxygen atoms, of $TFSI^-$ and amide (O_{amide}: O_U, O_{Ac}, O_{MAc}), in the first coordination shell of Li^+ cation and amine hydrogen atoms of amide (H_{amide}: H_U, H_{Ac}, H_{MAc}). Positions of the first minima of the RDF plots in figures 5 and 6 are chosen as the r_c distance in Eq. 7.

	$Li–O_{TFSI}$	$Li–O_{amide}$	$H_{amide}–O_{TFSI}$	$H_{amide}–O_{amide}$
URA	0.80	3.25	0.49	0.42
ACT	0.59	3.48	0.47	0.50
NMA	0.51	3.47	0.53	0.44

sults from bidentate coordinating $TFSI^-$ molecules in which two oxygen atoms of one $TFSI^-$ ion are bound to a single lithium ion, and the second one from monodentate $TFSI^-$ with only one oxygen atom bound to a cation. The notably more pronounced second peaks indicate that the $TFSI^-$ ions prefer monodentate coordination in these liquids. Furthermore, the number of $TFSI^-$ anions in the first coordination shell of a Li^+ cation, in Table S1 of the supplementary material, is equal to the number of O_{TFSI} atoms, indicating that on average only one of the four oxygen atoms of each anion coordinates to a Li^+ cation. Our results contradict the previously reported RDFs for the URA and ACT systems that show clear double peaks with considerably higher intensity[18,19]. In fact, the classical FF simulations significantly overestimate the cation–anion interaction while underestimating the cation–amide interaction.

The lithium ion RDFs in Fig. 7d show a distinct peak at a distance of around 2.9 Å. To better understand the nature of these close contacts between Li^+ cations, a series of cluster fragments were cut out from the collected trajectories and screened for configurations with a close distance of Li^+ ions. Fig. 8 shows selected snapshots of clusters from our simulations in which two Li^+ ions are at a close distance to each other. Investigating the selected structures reveals that in almost all cases, two of the surrounding amide molecules coordinate with both of the Li^+ ions. Furthermore, combined distribution functions (CDFs) of Li–Li and $Li–O_{amide}$ RDFs and the corresponding correlation plots, in Fig. S4 of the supplementary material, indicate that the short distance between Li^+ cations correlates with the close contact of Li^+ ions with O_{amide} atoms at 2.0 Å. On the other hand, the CDF plots of Li–Li and $Li–O_{TFSI}$ RDFs, in Fig. S5 of the supplementary material, show that such a correlation is absent for Li^+ interaction with oxygen atoms of the anion. Ad-

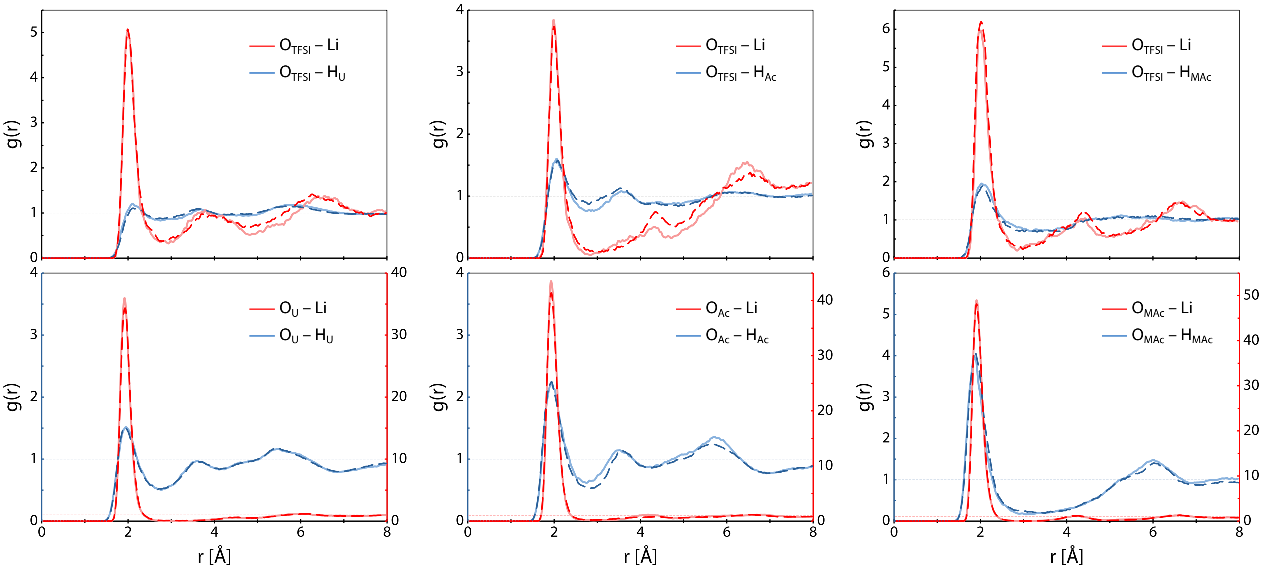

FIG. 4. Selected radial distribution functions, $g(r)$, from FPMD simulations (solid lines) are compared to RDFs from MLIP simulations (dashed lines) in the URA system (left), ACT system (middle), and NMA system (right). Atom labels are shown in Fig. 1.

ditionally, the close approach of Li^+ ions increases the possibility of hydrogen bond formation between the coordinating amide molecules. These findings imply that the close distance of Li^+ cations in these DEEs is mediated by the surrounding amide molecules. Previous simulation studies of the URA system using the OPLS-AA force field by Nandy *et al.*[19] and Lesch *et al.*[13] have shown that the first peak of the lithium–lithium RDF appears at a larger distance of about 4.0 Å with a significantly lower intensity compared to our results. Li *et al.*'s[18] results from MD simulations of the ACT system show no sign of close contact between lithium ions, and only a weak peak at 3.5 Å is reported for a lower acetamide to salt ratio. These results can be attributed to the absence of charge transfer and polarization effects in FF simulations, which significantly mitigate the electrostatic repulsion between the lithium ions[83]. We can confirm that this effect is not an artifact of the MLIP simulations, as similar outcomes are observed in our reference FPMD simulations (see Fig. S6 of the supplementary material).

The molecular conformation of the $TFSI^-$ anion in the studied DEEs was investigated using the CDFs, $g(r, \phi)$, in Fig. 9. The radial axis r denotes the distance between the Li^+ cation and the CoM of $TFSI^-$ anion, and the angular axis ϕ denotes the torsional angle between the two sulfur–carbon bonds of the $TFSI^-$ anion. We assign the ranges $0° \leq \phi \leq 90°$, $90° < \phi \leq 120°$, and $120° < \phi \leq 180°$ to the *cis*, *gauche*, and *trans* conformations, respectively. The contour plots in the top panels of Fig. 9 illustrate that three different conformations of the anion coexist in these liquids, although the *gauche* and *trans* conformations are notably more abundant. It has been shown that the energy barrier between the *trans* and *cis* conformations of TFSI in room-temperature ionic liquids is only 2–3.5 kJ mol^{-1}, which facilitates rapid conformational dynamics[84]. The two distinct high-intensity regions in the CDF plots in the $120°$ to $150°$ range correspond to the two main peaks of Li–TFSI RDFs in Fig. 7. The corresponding correlation plots in the bottom panels of Fig. 9 depict a more detailed picture of the r and ϕ relation. At short Li–TFSI distances of 3–4 Å, two distinct areas with positive correlation are visible, which are less pronounced in the NMA system. The shorter distance of a Li^+ cation to the anion's CoM up to 3.5 Å correlates with the *trans* conformation of TFSI in the $135°$ to $180°$ range, while the Li–TFSI distances of 3.5–4 Å correlate with the *gauche* and partly *cis* conformations. These can be assigned to a bidentate coordination of a Li^+ cation by the anion in *trans* and *gauche*/*cis* conformations, respectively. The strongest correlation, however, can be seen for the Li–TFSI distances of 4–5 Å and the *trans* conformation of the anion with torsional angles between $120°$ and $150°$, which as discussed earlier can be assigned to a monodentate coordination of a Li^+ cation by the anion.

In Fig. 10, the spatial distributions of CoM of cation, anion, and amide around a central $TFSI^-$ anion and an amide molecule are shown as isodensity surfaces. In agreement with the RDFs, the Li^+ cations form the closest coordination shell around the anion in all three DEEs, and the preferred coordination sites for the Li^+ cation on both the $TFSI^-$ and the amide molecule are the oxygen atoms. The density clouds of amide molecules around the central $TFSI^-$ or amide also correlates with those of the Li^+ cation. In panels d to f, the presence of density clouds of the anion and amide molecules close to the *cis* and *trans* hydrogen atoms of the amine groups, indicates the formation of hydrogen bonds between these species. Moreover, small density clouds of Li^+ cations are also visible on the sides and below the central amide molecules, which correlate with the density clouds of $TFSI^-$ and amide.

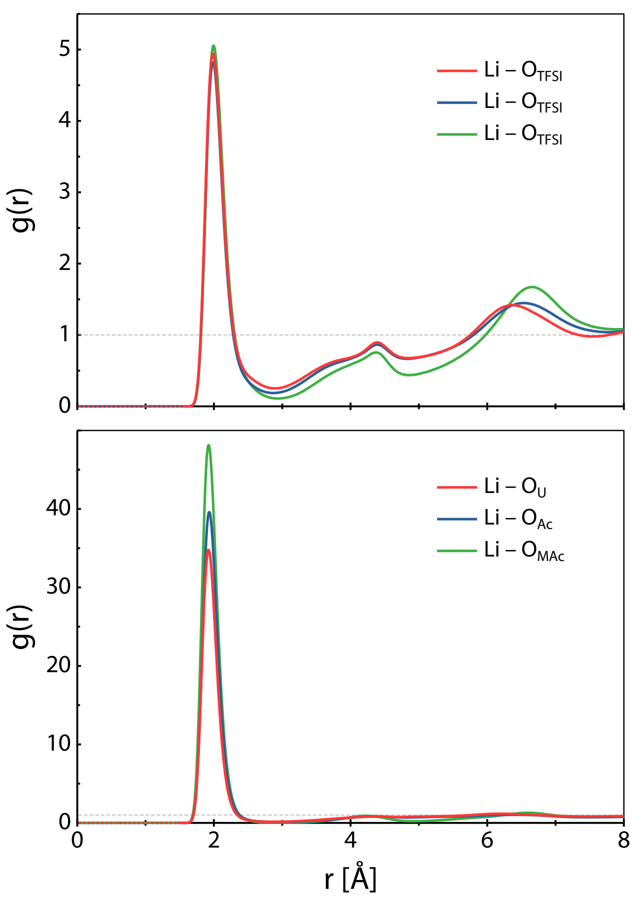

FIG. 5. Radial distribution functions, $g(r)$, of oxygen atoms, of TFSI$^-$ (top) and amide (bottom), around Li$^+$ cation in the URA system (red), ACT system (blue), and NMA system (green). Atom labels are shown in Fig. 1.

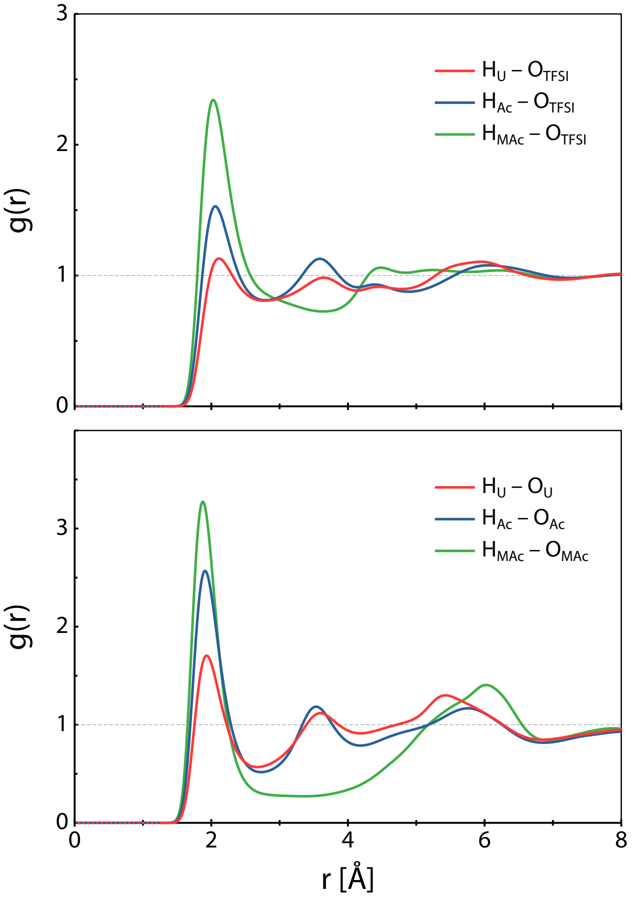

FIG. 6. Radial distribution functions, $g(r)$, of oxygen atoms, of TFSI$^-$ (top) and amide (bottom), around amine hydrogen atoms of amide in the URA system (red), ACT system (blue), and NMA system (green). Atom labels are shown in Fig. 1.

C. Dynamic and Transport Properties

We begin our analysis of the dynamics of the studied DEEs by comparing the computed velocity autocorrelation functions (VACFs),

$$A(t) = \frac{\langle \boldsymbol{v}_i(t) \cdot \boldsymbol{v}_i(0) \rangle_{i,t}}{\langle v_i^2 \rangle}, \tag{8}$$

where $\boldsymbol{v}_i(t)$ denotes the velocity of the CoM of particle i at any specific time, with the mean square velocities, $\langle v_i^2 \rangle$, as normalization factor. The VACFs in Fig. 11 show a similar Li$^+$ ion dynamics at short times in these DEEs, characterized by fast oscillations, which can be attributed to the back-and-forth motion of the cation surrounded by the amide molecules and the anions[30,85]. In the case of the TFSI$^-$ anion, the VACFs have a slower decay in the NMA and ACT systems compared to that of the URA, meaning that the anions maintain their initial momentum slightly longer in these systems. The same trend is also visible for the amide molecules, albeit to a lesser extent.

The self-diffusion coefficients (D) are estimated from an exponential fit to the running integral of the VACFs from the following Green–Kubo equation and are presented in Table II,

$$D = \frac{1}{3} \int_0^\infty \langle \boldsymbol{v}_i(t) \cdot \boldsymbol{v}_i(0) \rangle_{i,t} dt. \tag{9}$$

The self-diffusion coefficients are also estimated from the mean-square-displacement (MSD) of the CoM in Fig. 12 using the following Einstein equation,

$$D = \lim_{t \to \infty} \frac{1}{6t} \left\langle |\boldsymbol{r}_i(t) - \boldsymbol{r}_i(0)|^2 \right\rangle_{i,t}, \tag{10}$$

where $\boldsymbol{r}_i(t)$ is the position of the CoM of particle i at any specific time. Self-diffusion coefficients are obtained from a linear fit to the MSD plots, and are presented in Table S2 of the supplementary material.

The three components of studied DEEs have the fastest diffusivity in the NMA mixture, followed by those in the ACT and URA mixtures, respectively. This results align with the reported

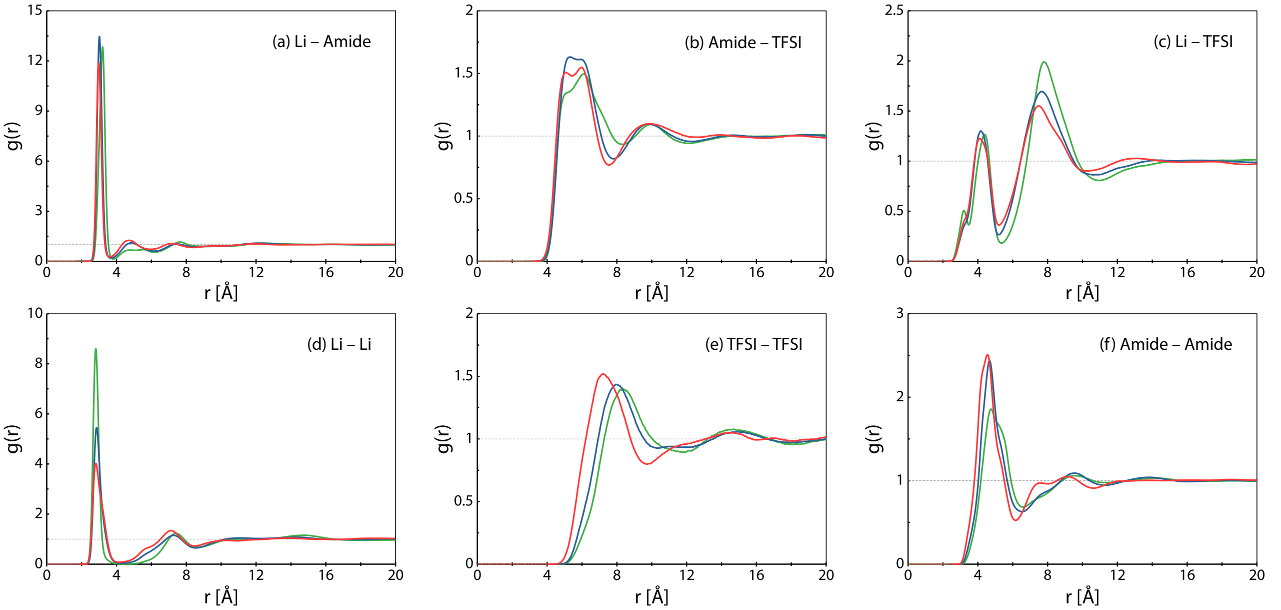

FIG. 7. Center-of-mass radial distribution functions, $g(r)$, of Li^+ cation, $TFSI^-$ anion and amide, in the URA system (red), ACT system (blue), and NMA system (green).

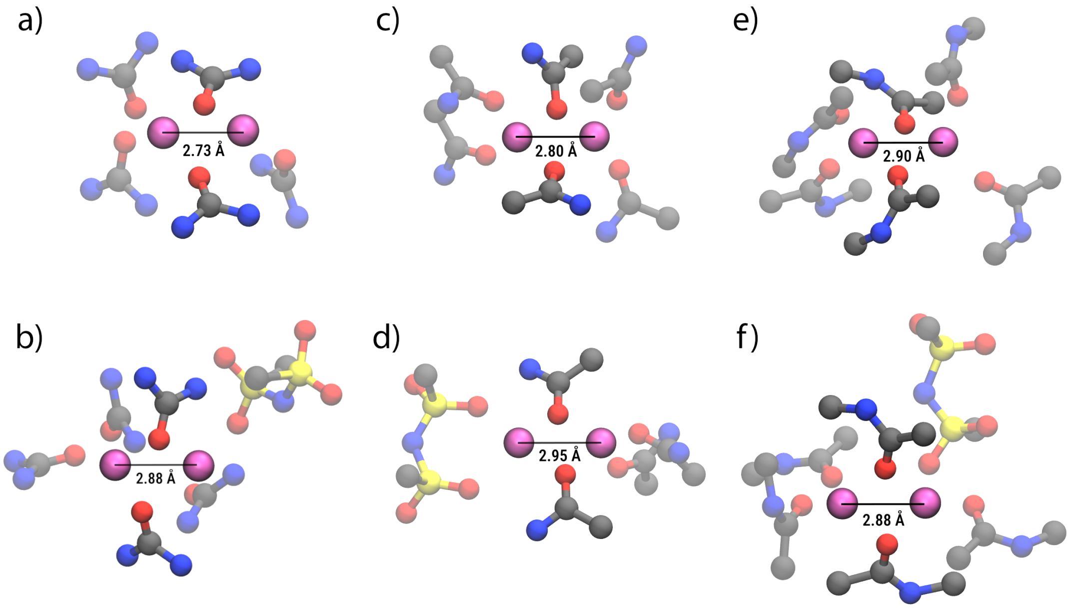

FIG. 8. Snapshot of cluster fragments in which two Li^+ cations are at close distance of one another in the URA system (a, b), ACT system (c, d), and NMA system (e, f). The two amide molecules that coordinate with both of the Li^+ cations are highlighted. The fluorine atoms of the $TFSI^-$ anion and the hydrogen atoms of amide molecules are not shown for better illustration.

viscosity trend in these liquids. The Li^+ cations and amide molecules have similar diffusion coefficients in the URA mixture and larger than that of the $TFSI^-$ anions. The D_{amide}/D_{Li} ratios of ≈ 1.5 and 1.7 for the ACT and NMA mixtures, respectively, indicate that the amide molecules have a faster diffusivity than the Li^+ cations in these liquids. Slower diffusion of Li^+ ions relative to amide molecules can be attributed to the larger hydrodynamic radius of a coordinated Li^+ cation compared to a free amide molecule[20]. These results also align with the obtained coordination numbers of amide molecules with a Li^+ ion, since on average a larger number of acetamide and N-methylacetamide molecules coordinate with a Li^+ cation, and

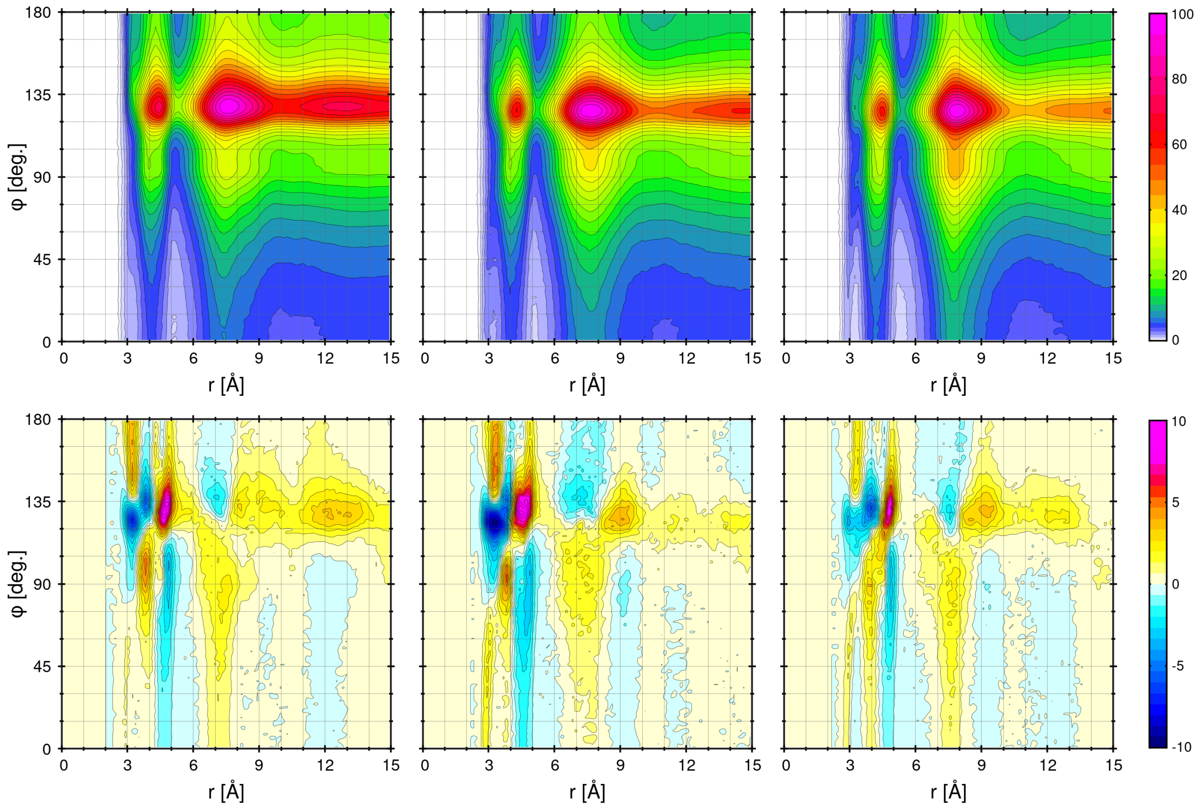

FIG. 9. Combined radial/torsional distribution functions, $g(r, \phi)$ (top row), and the corresponding correlation plots (bottom row), for the URA system (left), ACT system (middle), and NMA system (right). Radial axis r denotes the center-of-mass distance between the Li^+ cation and the $TFSI^-$ anion and ϕ denotes the torsional angle between the two S – C bonds of the $TFSI^-$ anion.

the fact that N-methylacetamide has a larger size compared to urea and acetamide.

The self-diffusion coefficients of cation and anion can also be employed to calculate the cationic transport number, which is defined as $t^+ = D_+/(D_+ + D_-)$. The cationic transport number provides an expression for the amount of transported cations, in the limit of negligible ion correlations, and is an important quantity in electrolyte solutions for electrochemical applications such as LIBs[86]. In Table II, a value of $t^+ > 0.5$ for the URA system indicates that the Li^+ cations have a higher diffusivity compared to the $TFSI^-$ anions, which is a characteristic of effective electrolyte solutions[87]. The value of $t^+ \approx 0.5$ for the ACT system implies that the diffusivity of anions and cations is roughly comparable in this DEE. The obtained value of cationic transport number of slightly less than 0.5 in the NMA system shows that anions have a higher diffusivity compared to the cations, indicating that anions might have a larger contribution to the ionic conductivity in the NMA electrolyte. Crabb et al. have shown that for a series of LiTFSI-based electrolytes, the Li^+ transport number t^+ correlates with the Li–TFSI coordination number[20]. Interestingly, the same correlation between t^+ and the $TFSI^-$ coordination number with the Li^+ cation can also be observed for the studied DEEs in this work, in which the D_{Li}/D_{TFSI} ratio becomes increasingly smaller with decreasing Li–TFSI coordination number. Moreover, the descriptor introduced by Crabb et al.[20], defined as the Li–solvent interaction energy divided by the viscosity of the electrolyte, is shown to strongly correlate with the Li^+ transport ratio of Borodin and Smith[22], which itself is an identifier for the Li^+ cation transport mechanism in the studied electrolytes. Their obtained results support the hypotheses that higher viscosity will decrease the contributions from a vehicular transport mechanism, whereas stronger interactions between the solvent and Li^+ will increase the contributions from a vehicular mechanism. Compellingly, similar conclusions can be drawn regarding the Li^+ transport mechanism in the studied DEEs in this work. The lower viscosity and slower diffusion of Li^+ ions compared to the $TFSI^-$ counterions, indicated by the $t^+ < 0.5$, suggest a more vehicular transport mechanism of Li^+ ions in the NMA electrolyte, in which the Li^+ cation diffuses along with its coordination shell. However, a higher viscosity and faster diffusion of Li^+ ions than anions in the URA system indicate that a solvent-exchange mechanism might have a larger contribution to Li^+ ion transport in this DEE. The slightly higher viscosity of the ACT mixture compared to the NMA, and a comparable diffusivity of Li^+ cations and $TFSI^-$ anions imply that a vehicular mechanism might have an equal contribution to lithium ion transport as a solvent-exchange mechanism in the ACT system[21].

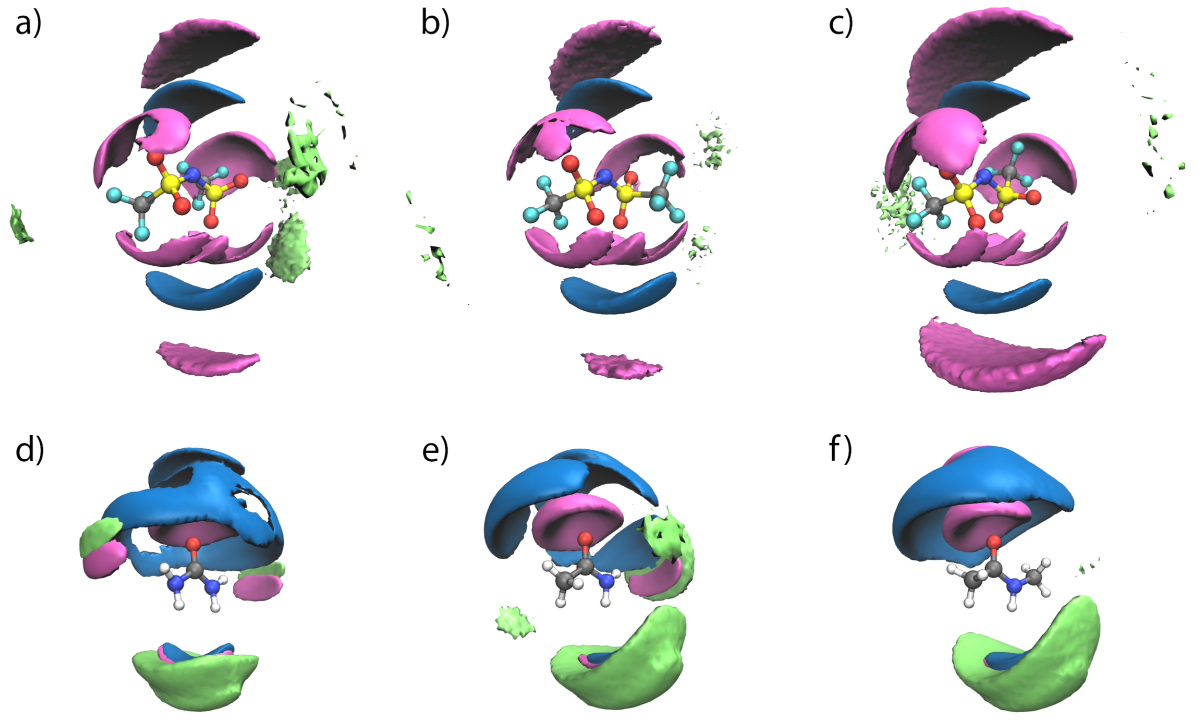

FIG. 10. Spatial distribution of center-of-mass isodensity surfaces around a TFSI$^-$ anion, and an amide molecule in the URA system (a, d), the ACT system (b, e), and the NMA system (c, f). The density clouds of Li, TFSI, and amide are colored purple, green, and blue, respectively. The relative number densities N, with respect to their average bulk densities, of different species in panels a to c are N(Li)=4, N(TFSI)=2.4, and N(amide)=4, and those in panels d to f are N(Li)=4, N(TFSI)=2.8, and N(amide)=4.

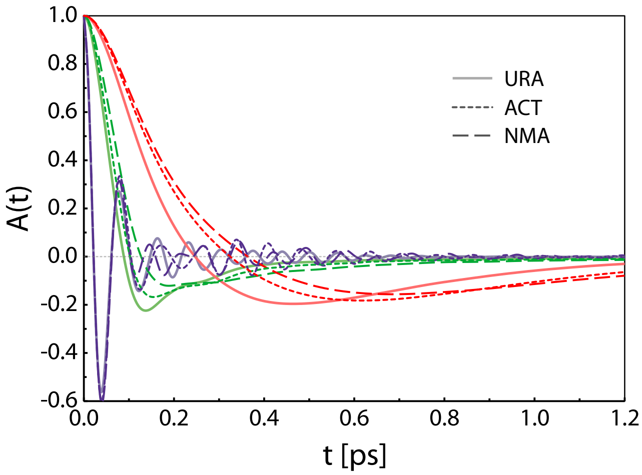

FIG. 11. Center-of-mass velocity autocorrelation functions, $A(t)$, of Li$^+$ cation (purple), TFSI$^-$ anion (red), and amide (green) as a function of correlation time.

To further clarify the relation between the Li–amide dynamics and Li$^+$ transport, the lithium–amide lifetime, as the average time that an amide molecule remains coordinated to a Li$^+$ ion, and the average rotational relaxation time of the amide molecules were computed. The lifetime ($\tau_{\text{Li–amide}}$) is estimated from the integral of a poly-exponential function fitted to the following pair existence autocorrelation function[22],

$$P(t) = \frac{\langle h_{ij}(t) h_{ij}(0) \rangle_{ij,t}}{\langle h_{ij}(0)^2 \rangle_{ij,t}}, \tag{11}$$

where $h_{ij}(t)$ is equal to one if an amide molecule j is present in the first coordination shell of a Li$^+$ cation i (i.e. Li–O(amide) distance $\leq$ 3 Å), and is zero otherwise. The rotational relaxation time (τ_R) is estimated from an integral over the autocorrelation function, $\langle \boldsymbol{u}_i(t) \cdot \boldsymbol{u}_i(0) \rangle_{i,t}$, where $\boldsymbol{u}_i(t)$ is defined as the vector pointing from the carbon atom to the oxygen atom of the carbonyl group (C→O) in an amide molecule at any specific time. The pair existence and rotational relaxation time autocorrelation function are presented in Fig. S7 of the supplementary material. The $\tau_{\text{Li–amide}}/\tau_\text{R}$ ratio can be considered a factor associated with the Li$^+$ ion transport mechanism. If $\tau_{\text{Li–amide}}/\tau_\text{R}$ is less than one, solvent exchange occurs before the rotational relaxation of amides, hence Li$^+$ transport would be faster than the rearrangement of the surrounding amide molecules. Consequently, the network structure of surrounding amide molecules would be maintained during Li$^+$ ion transport, indicating a solvent-exchange transport mechanism. However, if $\tau_{\text{Li–amide}}/\tau_\text{R}$ is greater than one, the reorientation dynamics of amide molecules are faster than solvent

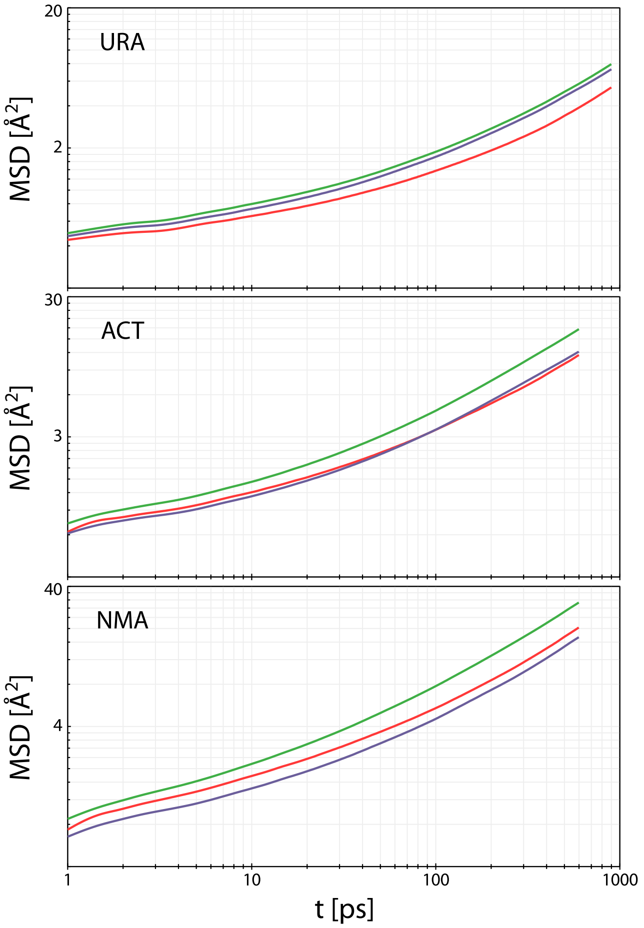

FIG. 12. The mean-square displacement (MSD) of the center-of-mass of Li^+ cation (purple), $TFSI^-$ anion (red), and amide (green) as a function of time-lag (t). We used 30% of the trajectory length as the maximum correlation depth. Self-diffusion coefficients are calculated from a linear fit to the second half of the plots.

exchange. This means the Li^+ ion would be transported along with local structural changes as a solvated Li^+ complex in the electrolyte, which can be interpreted as vehicular transport[88]. The computed Li–amide lifetimes, amide rotational relaxation times, and the corresponding ratios are listed in Table II. The obtained $\tau_{\text{Li–amide}}/\tau_{\text{R}}$ ratio of 0.4 for the URA system indicates a solvent-exchange dominated transport of the Li^+ ion in this DEE, while the value of 0.85 in the ACT electrolyte implies a more balanced contribution from both vehicular and exchange transport of the Li^+ cation. The estimated value of 1.76 in the NMA system also aligns with the discussed results in the previous section and suggests a more pronounced vehicular transport of Li^+ ion in this electrolyte.

The ionic conductivity of the studied DEEs was estimated by integrating the charge current autocorrelation function using the following Green–Kubo equation[85],

$$\sigma = \frac{1}{3k_BTV}\int_0^\infty \langle \boldsymbol{J}(t)\cdot\boldsymbol{J}(0)\rangle_t dt, \tag{12}$$

where k_B is the Boltzmann constant, T is the temperature, and V is the volume of the simulation box. The charge current $\boldsymbol{J}(t)$ defined as

$$\boldsymbol{J}(t) = e\sum_{i=1}^{N}\boldsymbol{v}_i(t), \tag{13}$$

where N is the total number of ions, and e and $\boldsymbol{v}_i(t)$ represent the elementary charge and the CoM velocity of the ith ion at time t, respectively. The ionic conductivity (σ) is computed from the long-time limit of an exponential decay function, fitted to the running integral of the charge current autocorrelation function of Eq. 12. It should be noted that evaluating the conductivity through this approach is challenging, as ionic conductivity is a collective dynamical property of the whole system and, for this reason, suffers from relatively high statistical uncertainty[89,90]. The ionic conductivity can also be estimated using the Nernst–Einstein expression from the self-diffusion coefficients of ionic species,

$$\sigma_{\text{NE}} = \frac{Ne^2}{k_BTV}(D_+ + D_-), \tag{14}$$

where N is the number of ion pairs in the simulation, and $D_\pm$ is the diffusion coefficients of the cation and anion. The Nernst–Einstein expression is based on the assumption of uncorrelated motion of ions, so it is only exact in the infinite dilution limit and will break down for highly concentrated systems and systems with a high degree of ion clustering[90]. Consequently, by considering the obtained values from the Green–Kubo approach as true conductivities, their deviation from Nernst–Einstein values can be interpreted as the degree of ion–ion correlation. The Green–Kubo and Nernst–Einstein conductivities, along with the corresponding ($\sigma/\sigma_{\text{NE}}$) ratios, are listed in Table III and compared to the experimentally reported values. The estimated values of the ionic conductivity (σ) from the MLIP-based simulations are approximately 40% lower than the experimentally reported values in all three electrolytes, demonstrating the ability of the MLIPs to accurately capture the conductivity trends in these DEEs. The NMA system has the highest ionic conductivity among the three DEEs, with a value $\approx$3 times larger than that of the URA system, while the ionic conductivity of the ACT system is close to that of the NMA system. Interestingly, the ratio of the experimentally reported viscosity values for the ACT[16] and NMA[17] systems is very close to the ratio of their ionic conductivities, further emphasizing the effect of viscosity on the ion transport mechanism in these DEEs. Furthermore, the corresponding $\sigma/\sigma_{\text{NE}}$ ratio in Table III shows a value close to one for the URA system, suggesting uncorrelated motion of counterions in this electrolyte. For the ACT and NMA electrolytes, a $\sigma/\sigma_{\text{NE}}$ value of less than one points to some degree of correlated motion between oppositely charged ions, which is more pronounced in the NMA system. These results also align with the obtained cation transport numbers, further supporting the discussed cation transport mechanisms in these DEEs.

The collective dynamics of the electrolyte's components at short timescales can be investigated through velocity cross-

TABLE II. Self-diffusion coefficients, D (10^{-11} m^2 s^{-1}) from the Green–Kubo equation for the three components of the DEEs, and the corresponding cation transport number t^+. The Li–amide lifetime, $\tau_{\text{Li–amide}}$ (ns), rotational relaxation time of the amide molecule, τ_{R} (ns), and their corresponding ratio.

	D_{Li}	D_{TFSI}	D_{amide}	t^+	$\tau_{\text{Li–amide}}$	τ_{R}	$\tau_{\text{Li–amide}}/\tau_{\text{R}}$
URA	1.07	0.70	1.11	0.60	0.63	1.53	0.41
ACT	3.19	3.01	4.72	0.51	0.60	0.71	0.85
NMA	4.92	5.67	8.60	0.46	0.88	0.50	1.76

TABLE III. The estimated values of ionic conductivity from MD simulations by the Green–Kubo approach (σ), the Nernst–Einstein equation (σ_{NE}) (using the Green–Kubo self-diffusion coefficients) and the reported experimental values (σ_{Exp}). α denotes the corresponding ratio ($\sigma/\sigma_{\text{NE}}$). Ionic conductivities have the unit of S m^{-1}.

	σ_{Exp}	σ	σ_{NE}	α
URA	0.32[15][a]	0.19	0.18	1.03
ACT	0.83[16][a]	0.48	0.51	0.94
NMA	0.92[17]	0.56	0.72	0.78

[a] Value is taken from the VTF plot of conductivity.

correlation functions (VCCFs). The time cross-correlation function between the initial velocity of a particle of type i and the latter velocities of particles of type j, initially located inside a spherical shell of radius R around the particle of type i, can be defined as

$$C(t) = \frac{\langle \boldsymbol{v}_j(t) \cdot \boldsymbol{v}_i(0) \rangle_r}{\left(\langle v_i^2 \rangle \langle v_j^2 \rangle \right)^{1/2}}, \tag{15}$$

where $\boldsymbol{v}_i(t)$ and $\boldsymbol{v}_j(t)$ are the velocity of the particles i and j at any specific time, $\langle v_i^2 \rangle$ and $\langle v_j^2 \rangle$ are the mean squared velocities of all particles of type i and j, respectively. $\langle \boldsymbol{v}_j(t) \cdot \boldsymbol{v}_i(0) \rangle_r$ is a restricted statistical average defined as

$$\frac{1}{N} \left\langle \sum_j \boldsymbol{v}_j(t) \cdot \boldsymbol{v}_i(0) \cdot u(R - r_{ij}(0)) \right\rangle_{i,t}, \tag{16}$$

where $u(x)$ is the step function, $r_{ij}(0)$ is the initial distance between the central particle i and a particle j, and N is the mean number of j particles in the spherical shell of a particle i. The cutoff radius R for species i and j is set to the position of the first minimum of the corresponding CoM RDF in Fig. 7. The computed VCCFs, $C(t)$, are plotted in Fig. 13, alongside the corresponding VACFs from Fig. 11. The initial rise of the VCCFs, with the decay of the corresponding VACFs, indicate the transfer of the initial momentum of the central particle to the neighboring particles. The decay of the functions after the first peak could be associated with the spread of the momentum to the particles in outer shells[91]. The VCCFs between particles of different type, in the top row of Fig. 11, are rather similar in all three DEEs. One noticeable difference is the slower decay of the TFSI–Amide function from the URA to ACT and NMA systems, which reach zero at 0.44 ps, 0.54 ps and 0.64 ps, respectively. The same trend, although to a lesser extent, is also visible in the Li–TFSI functions. The Li–Amide functions have the most pronounced first peak and distinct oscillations with a noticeable phase relation to the oscillations of the Li$^+$ VACF. The maxima of the Li–Amide function coincide with the minima of the Li$^+$ VACF, and vice versa, indicating a strongly coupled motion of Li$^+$ ions and amide molecules at short timescales up to ≈1 ps. The back-and-forth motion of the Li$^+$ ion alternately slows down and speeds up the amide molecules in their direction of movement. A small influence of the cation oscillations on the motion of anions is also visible in the Li–TFSI functions at short times up to 0.2 ps. The VCCFs of distinct same-type particles, in the bottom row of Fig. 11, show the strongest correlation between the distinct amide molecules. The Amide–Amide functions reach their maximum at the same time that amide molecules, on average, lose their initial momentum and the corresponding VACF becomes negative. The correlation functions between the distinct TFSI$^-$ anions reach their maximum shortly after the corresponding VACF becomes negative, suggesting that the heavier anions on average maintain their initially gained momentum for longer times. Moreover, the TFSI–TFSI functions show a smaller intensity and a slower rise and decay from the URA to ACT and NMA systems, indicating a more restricted transfer of momentum between neighboring anions in the latter. The cross-correlation functions between the Li$^+$ cations in close vicinity of each other show oscillations that are rather in phase with the oscillations of the Li$^+$ VACFs, and are notably more pronounced in the NMA system, followed by those in the ACT system. This suggests a coupled rocking motion of the neighboring Li$^+$ ions, which on average move in the same direction.

IV. SUMMARY AND CONCLUSIONS

The structure and dynamics of a series of DEEs based on LiTFSI salt and three amide molecules were studied by MD simulations using equivariant MLIPs. The interatomic potentials were trained on atomic configurations labeled with energies and atomic forces, initially sampled from short DFT-based FPMD simulations, using the Allegro[59] model, a strictly local many-body equivariant NNIP. We used an iterative active learning procedure based on calibrated uncertainties from model ensemble predictions combined with the conformal prediction method to identify under-represented parts of the configuration space in the initial training dataset and select the most infor-

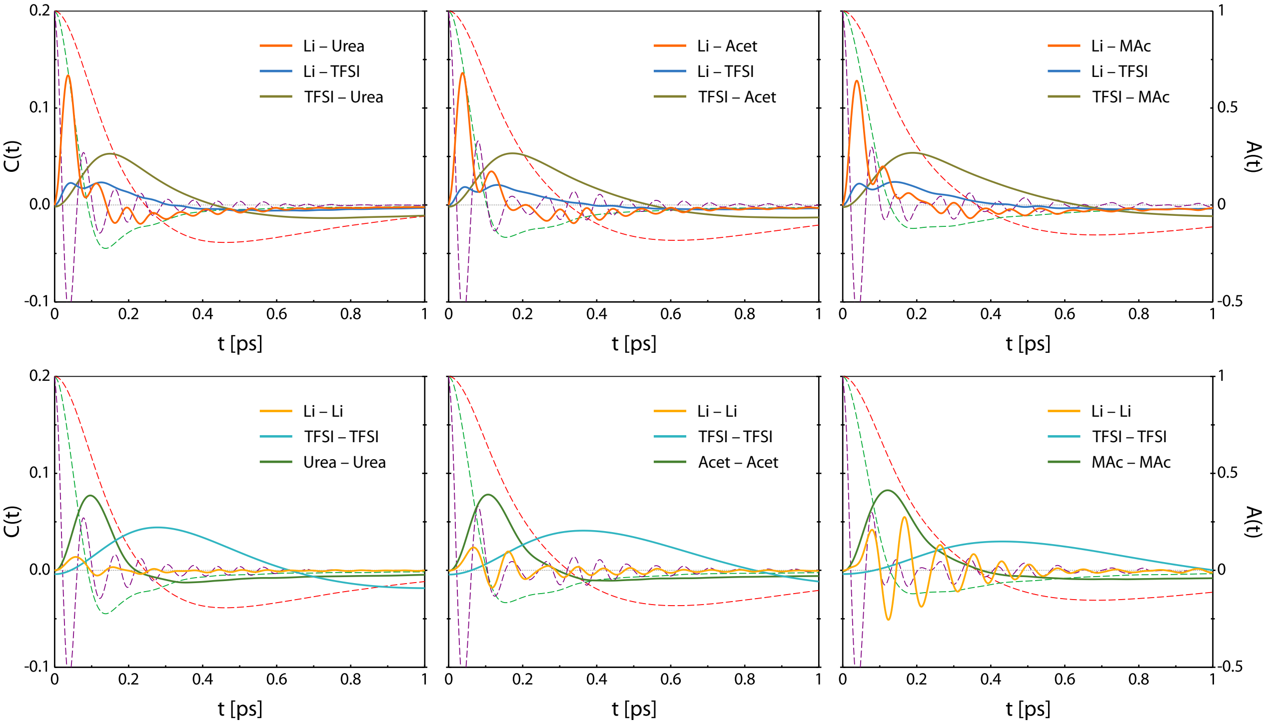

FIG. 13. Center-of-mass velocity cross-correlation functions, $C(t)$, of the three components of DEE in the URA system (left), ACT system (middle), and NMA system (right) as a function of correlation time. The dashed lines are the center-of-mass velocity autocorrelation functions, $A(t)$, of Li^+ cation (purple), $TFSI^-$ anion (red), and amide (green).

mative configurations to expand the training set. The trained MLIPs achieve remarkable accuracy in predicting energies and atomic forces for a set of test structures, and can successfully reproduce the structure and short-time dynamics of the DEEs compared to the reference FPMD simulations. The use of equivariant representations results in models that are more accurate and about an order of magnitude more data-efficient compared to invariant models in our pervious study[38], and require fewer active learning iterations to reach the desired accuracy. More importantly, they enable significantly more stable simulations, indicating superior generalization capabilities of MLIPs based on equivariant representations.

Investigating the structure of the liquids indicates that the strong interaction between the lithium cation and the oxygen atom of amide molecules effectively disrupt the crystal lattice of the LiTFSI salt and is the main driving force for the melting point depression in these DEEs. Furthermore, comparing the liquid structure from MD simulations of this work to previously reported results from FF simulations reveals that ion–ion interactions are not correctly captured by the FFs, as they tend to overestimate the attraction between counterions and repulsion between Li^+ cations.

The investigated dynamics and transport properties of different components of the studied DEEs, more specifically the obtained cationic transport numbers and the estimated $\tau_{\text{Li–amide}}/\tau_{\text{R}}$ ratios, combined with their viscosity and ionic conductivity trends, suggest a more structural transport mechanism for the lithium ion in the URA electrolyte through exchange of amide molecules. Meanwhile, the vehicular mechanism could have an increasingly larger contribution to lithium ion transport in the ACT and specifically NMA electrolytes.

SUPPLEMENTARY MATERIAL

The supporting information include details of the first-principles molecular dynamics simulations, additional data on elemental contribution to the error distribution of the predicted atomic forces, coordination numbers of different species in their first solvation shell, computed self-diffusion coefficients from the Einstein equation, and additional velocity autocorrelation, radial/combined distribution functions.

ACKNOWLEDGMENTS

The authors thank the German Research Foundation (DFG) for financial support (project ZA 606/8-1). Computational resources from the Center for Information Services and High Performance Computing (ZIH) of TU Dresden, and Scientific Computing at the University of Leipzig are gratefully acknowledged.

AUTHOR DECLARATIONS

Conflict of Interest

The authors have no conflicts to disclose.

Author Contributions

Omid Shayestehpour: Conceptualization (equal); Data curation (lead); Formal analysis (lead); Investigation (lead); Methodology (lead); Software (lead); Visualization (lead); Writing – original draft (lead); Writing – review & editing (equal). **Stefan Zahn**: Conceptualization (equal); Funding acquisition (lead); Methodology (supporting); Project administration (lead); Supervision (lead); Writing – review & editing (equal).

DATA AVAILABILITY

The data that support the findings of this study will be available upon publication at 10.5281/zenodo.13254497.

REFERENCES

[1] A. P. Abbott, G. Capper, D. L. Davies, R. K. Rasheed, and V. Tambyrajah, "Novel solvent properties of choline chloride/urea mixtures," Chem. Commun. , 70–71 (2003).

[2] Q. Zhang, K. De Oliveira Vigier, S. Royer, and F. Jérôme, "Deep eutectic solvents: syntheses, properties and applications," Chem. Soc. Rev. **41**, 7108–7146 (2012).

[3] M. A. R. Martins, S. P. Pinho, and J. A. P. Coutinho, "Insights into the nature of eutectic and deep eutectic mixtures," Journal of Solution Chemistry **48**, 962–982 (2019).

[4] E. L. Smith, A. P. Abbott, and K. S. Ryder, "Deep eutectic solvents (DESs) and their applications," Chemical Reviews **114**, 11060–11082 (2014), pMID: 25300631.

[5] B. B. Hansen, S. Spittle, B. Chen, D. Poe, Y. Zhang, J. M. Klein, A. Horton, L. Adhikari, T. Zelovich, B. W. Doherty, B. Gurkan, E. J. Maginn, A. Ragauskas, M. Dadmun, T. A. Zawodzinski, G. A. Baker, M. E. Tuckerman, R. F. Savinell, and J. R. Sangoro, "Deep eutectic solvents: A review of fundamentals and applications," Chemical Reviews **121**, 1232–1285 (2021), pMID: 33315380.

[6] A. K. Halder and M. N. D. S. Cordeiro, "Probing the environmental toxicity of deep eutectic solvents and their components: An in silico modeling approach," ACS Sustainable Chemistry & Engineering **7**, 10649–10660 (2019).

[7] J. Wu, Q. Liang, X. Yu, Q.-F. Lü, L. Ma, X. Qin, G. Chen, and B. Li, "Deep eutectic solvents for boosting electrochemical energy storage and conversion: A review and perspective," Advanced Functional Materials **31**, 2011102 (2021), https://onlinelibrary.wiley.com/doi/pdf/10.1002/adfm.202011102.

[8] A. Sharma, R. Sharma, R. C. Thakur, and L. Singh, "An overview of deep eutectic solvents: Alternative for organic electrolytes, aqueous systems & ionic liquids for electrochemical energy storage," Journal of Energy Chemistry **82**, 592–626 (2023).

[9] M. H. Chakrabarti, F. S. Mjalli, I. M. AlNashef, M. A. Hashim, M. A. Hussain, L. Bahadori, and C. T. J. Low, "Prospects of applying ionic liquids and deep eutectic solvents for renewable energy storage by means of redox flow batteries," Renewable and Sustainable Energy Reviews **30**, 254–270 (2014).

[10] Q. Xu, L. Qin, Y. Ji, P. Leung, H. Su, F. Qiao, W. Yang, A. Shah, and H. Li, "A deep eutectic solvent (DES) electrolyte-based vanadium-iron redox flow battery enabling higher specific capacity and improved thermal stability," Electrochimica Acta **293**, 426–431 (2019).

[11] W. Dean, M. Muñoz, J. Noh, Y. Liang, W. Wang, and B. Gurkan, "Tuning and high throughput experimental screening of eutectic electrolytes with co-solvents for redox flow batteries," Electrochimica Acta **474**, 143517 (2024).

[12] O. Geiculescu, D. DesMarteau, S. Creager, O. Haik, D. Hirshberg, Y. Shilina, E. Zinigrad, M. Levi, D. Aurbach, and I. Halalay, "Novel binary deep eutectic electrolytes for rechargeable Li-ion batteries based on mixtures of alkyl sulfonamides and lithium perfluoroalkylsulfonimide salts," Journal of Power Sources **307**, 519–525 (2016).

[13] V. Lesch, A. Heuer, B. R. Rad, M. Winter, and J. Smiatek, "Atomistic insights into deep eutectic electrolytes: the influence of urea on the electrolyte salt LiTFSI in view of electrochemical applications," Phys. Chem. Chem. Phys. **18**, 28403–28408 (2016).

[14] P. Jiang, L. Chen, H. Shao, S. Huang, Q. Wang, Y. Su, X. Yan, X. Liang, J. Zhang, J. Feng, and Z. Liu, "Methylsulfonylmethane-based deep eutectic solvent as a new type of green electrolyte for a high-energy-density aqueous lithium-ion battery," ACS Energy Letters **4**, 1419–1426 (2019), https://doi.org/10.1021/acsenergylett.9b00968.

[15] H. Liang, H. Li, Z. Wang, F. Wu, L. Chen, and X. Huang, "New binary room-temperature molten salt electrolyte based on urea and LiTFSI," The Journal of Physical Chemistry B **105**, 9966–9969 (2001), https://doi.org/10.1021/jp0119779.

[16] Y. Hu, H. Li, X. Huang, and L. Chen, "Novel room temperature molten salt electrolyte based on LiTFSI and acetamide for lithium batteries," Electrochemistry Communications **6**, 28–32 (2004).

[17] A. Boisset, S. Menne, J. Jacquemin, A. Balducci, and M. Anouti, "Deep eutectic solvents based on N-methylacetamide and a lithium salt as suitable electrolytes for lithium-ion batteries," Phys. Chem. Chem. Phys. **15**, 20054–20063 (2013).

[18] S. Li, Z. Cao, Y. Peng, L. Liu, Y. Wang, S. Wang, J.-Q. Wang, T. Yan, X.-P. Gao, D.-Y. Song, and P.-W. Shen, "Molecular dynamics simulation of LiTFSI-acetamide electrolytes: Structural properties," The Journal of Physical Chemistry B **112**, 6398–6410 (2008), pMID: 18444674, https://doi.org/10.1021/jp710898h.

[19] A. Nandy and J. Smiatek, "Mixtures of litfsi and urea: ideal thermodynamic behavior as key to the formation of deep eutectic solvents?" Phys. Chem. Chem. Phys. **21**, 12279–12287 (2019).

[20] E. Crabb, A. Aggarwal, R. Stephens, Y. Shao-Horn, G. Leverick, and J. C. Grossman, "Electrolyte dependence of Li+ transport mechanisms in small molecule solvents from classical molecular dynamics," The Journal of Physical Chemistry B **128**, 3427–3441 (2024), pMID: 38551621, https://doi.org/10.1021/acs.jpcb.3c07999.

[21] O. Borodin and G. D. Smith, "LiTFSI structure and transport in ethylene carbonate from molecular dynamics simulations," The Journal of Physical Chemistry B **110**, 4971–4977 (2006), pMID: 16526738, https://doi.org/10.1021/jp056249q.

[22] O. Borodin and G. D. Smith, "Li+ transport mechanism in oligo(ethylene oxide)s compared to carbonates," Journal of Solution Chemistry **36**, 803–813 (2007).

[23] Z. Li, O. Borodin, G. D. Smith, and D. Bedrov, "Effect of organic solvents on Li+ ion solvation and transport in ionic liquid electrolytes: A molecular dynamics simulation study," The Journal of Physical Chemistry B **119**, 3085–3096 (2015), pMID: 25592777, https://doi.org/10.1021/jp510644k.

[24] T. P. Liyana-Arachchi, J. B. Haskins, C. M. Burke, K. M. Diederichsen, B. D. McCloskey, and J. W. Lawson, "Polarizable molecular dynamics and experiments of 1,2-dimethoxyethane electrolytes with lithium and sodium salts: Structure and transport properties," The Journal of Physical Chemistry B **122**, 8548–8559 (2018), pMID: 30130409, https://doi.org/10.1021/acs.jpcb.8b03445.

[25] S. Gabl, C. Schröder, and O. Steinhauser, "Computational studies of ionic liquids: Size does matter and time too," The Journal of Chemical Physics **137**, 094501 (2012), https://pubs.aip.org/aip/jcp/article-pdf/doi/10.1063/1.4748352/15452805/094501_1_online.pdf.

[26] C. Cadena, Q. Zhao, R. Q. Snurr, and E. J. Maginn, "Molecular modeling and experimental studies of the thermodynamic and transport properties of pyridinium-based ionic liquids," The Journal of Physical Chemistry B **110**, 2821–2832 (2006), pMID: 16471891.

[27] T. Yan, Y. Wang, and C. Knox, "On the dynamics of ionic liquids: Comparisons between electronically polarizable and nonpolarizable models II," The Journal of Physical Chemistry B **114**, 6886–6904 (2010), pMID: 20443608.

[28] A. d. O. Cavalcante, M. C. C. Ribeiro, and M. S. Skaf, "Polarizability effects on the structure and dynamics of ionic liquids," The Journal of Chemical Physics **140**, 144108 (2014), https://pubs.aip.org/aip/jcp/article-pdf/doi/10.1063/1.4869143/15477589/144108_1_online.pdf.

[29] K.-j. Jeong, J. G. McDaniel, and A. Yethiraj, "Deep eutectic solvents: Molecular simulations with a first-principles polarizable force field," The Journal of Physical Chemistry B **125**, 7177–7186 (2021), pMID: 34181852.

[30] O. Shayestehpour and S. Zahn, "Ion correlation in choline chloride–urea deep eutectic solvent (reline) from polarizable molecular dynamics simulations," The Journal of Physical Chemistry B **126**, 3439–3449 (2022), pMID: 35500254.

[31] M. Eckhoff and J. Behler, "From molecular fragments to the bulk: Development of a neural network potential for MOF-5," Journal of Chemical Theory and Computation **15**, 3793–3809 (2019), pMID: 31091097, https://doi.org/10.1021/acs.jctc.8b01288.

[32] V. L. Deringer, N. Bernstein, G. Csányi, C. Ben Mahmoud, M. Ceriotti, M. Wilson, D. A. Drabold, and S. R. Elliott, "Origins of structural and electronic transitions in disordered silicon," Nature **589**, 59–64 (2021).

[33] S. L. Bore and F. Paesani, "Realistic phase diagram of water from "first principles" data-driven quantum simulations," Nature Communications **14**, 3349 (2023).

[34] H. Zhang, V. Juraskova, and F. Duarte, "Modelling chemical processes in explicit solvents with machine learning potentials," Nature Communications **15**, 6114 (2024).

[35] H. Montes-Campos, J. Carrete, S. Bichelmaier, L. M. Varela, and G. K. H. Madsen, "A differentiable neural-network force field for ionic liquids," Journal of Chemical Information and Modeling **62**, 88–101 (2022), pMID: 34941253.

[36] J. P. Stoppelman and J. G. McDaniel, "Physics-based, neural network force fields for reactive molecular dynamics: Investigation of carbene formation from [EMIM+][OAc-]," The Journal of Chemical Physics **155**, 104112 (2021), https://pubs.aip.org/aip/jcp/article-pdf/doi/10.1063/5.0063187/16154308/104112_1_online.pdf.

[37] S. Dajnowicz, G. Agarwal, J. M. Stevenson, L. D. Jacobson, F. Ramezanghorbani, K. Leswing, R. A. Friesner, M. D. Halls, and R. Abel, "High-dimensional neural network potential for liquid electrolyte simulations," The Journal of Physical Chemistry B **126**, 6271–6280 (2022), pMID: 35972463, https://doi.org/10.1021/acs.jpcb.2c03746.

[38] O. Shayestehpour and S. Zahn, "Efficient molecular dynamics simulations of deep eutectic solvents with first-principles accuracy using machine learning interatomic potentials," Journal of Chemical Theory and Computation **19**, 8732–8742 (2023), pMID: 37972596, https://doi.org/10.1021/acs.jctc.3c00944.

[39] F. Zills, M. R. Schäfer, S. Tovey, J. Kästner, and C. Holm, "Machine learning-driven investigation of the structure and dynamics of the BMIM-BF4 room temperature ionic liquid," Faraday Discuss. (2024), 10.1039/D4FD00025K.

[40] Z. A. H. Goodwin, M. B. Wenny, J. H. Yang, A. Cepellotti, J. Ding, K. Bystrom, B. R. Duschatko, A. Johansson, L. Sun, S. Batzner, A. Musaelian, J. A. Mason, B. Kozinsky, and N. Molinari, "Transferability and accuracy of ionic liquid simulations with equivariant machine learning interatomic potentials," The Journal of Physical Chemistry Letters **15**, 7539–7547 (2024), pMID: 39023916, https://doi.org/10.1021/acs.jpclett.4c01942.

[41] A. Glielmo, P. Sollich, and A. De Vita, "Accurate interatomic force fields via machine learning with covariant kernels," Phys. Rev. B **95**, 214302 (2017).

[42] S. Chmiela, A. Tkatchenko, H. E. Sauceda, I. Poltavsky, K. T. Schütt, and K.-R. Müller, "Machine learning of accurate energy-conserving molecular force fields," Science Advances **3**, e1603015 (2017), https://www.science.org/doi/pdf/10.1126/sciadv.1603015.

[43] F. A. Faber, A. S. Christensen, B. Huang, and O. A. von Lilienfeld, "Alchemical and structural distribution based representation for universal quantum machine learning," The Journal of Chemical Physics **148**, 241717 (2018), https://pubs.aip.org/aip/jcp/article-pdf/doi/10.1063/1.5020710/16654916/241717_1_online.pdf.

[44] R. Drautz, "Atomic cluster expansion for accurate and transferable interatomic potentials," Phys. Rev. B **99**, 014104 (2019).

[45] A. P. Bartók, M. C. Payne, R. Kondor, and G. Csányi, "Gaussian approximation potentials: The accuracy of quantum mechanics, without the electrons," Phys. Rev. Lett. **104**, 136403 (2010).

[46] J. Vandermause, S. B. Torrisi, S. Batzner, Y. Xie, L. Sun, A. M. Kolpak, and B. Kozinsky, "On-the-fly active learning of interpretable bayesian force fields for atomistic rare events," npj Computational Materials **6**, 20 (2020).

[47] J. Behler, "Representing potential energy surfaces by high-dimensional neural network potentials," Journal of Physics: Condensed Matter **26**, 183001 (2014).

[48] S. A. Ghasemi, A. Hofstetter, S. Saha, and S. Goedecker, "Interatomic potentials for ionic systems with density functional accuracy based on charge densities obtained by a neural network," Phys. Rev. B **92**, 045131 (2015).

[49] N. Artrith and A. Urban, "An implementation of artificial neural-network potentials for atomistic materials simulations: Performance for TiO2," Computational Materials Science **114**, 135–150 (2016).

[50] J. S. Smith, O. Isayev, and A. E. Roitberg, "ANI-1: an extensible neural network potential with DFT accuracy at force field computational cost," Chem. Sci. **8**, 3192–3203 (2017).

[51] K. Yao, J. E. Herr, D. W. Toth, R. Mckintyre, and J. Parkhill, "The TensorMol-0.1 model chemistry: a neural network augmented with long-range physics," Chem. Sci. **9**, 2261–2269 (2018).

[52] K. T. Schütt, H. E. Sauceda, P.-J. Kindermans, A. Tkatchenko, and K.-R. Müller, "SchNet – A deep learning architecture for molecules and materials," The Journal of Chemical Physics **148**, 241722 (2018).

[53] J. Han, L. Zhang, R. Car, and W. E, "Deep potential: A general representation of a many-body potential energy surface," Communications in Computational Physics **23**, 629–639 (2018).

[54] V. Zaverkin, D. Holzmüller, I. Steinwart, and J. Kästner, "Fast and sample-efficient interatomic neural network potentials for molecules and materials based on Gaussian moments," Journal of Chemical Theory and Computation **17**, 6658–6670 (2021), pMID: 34585927, https://doi.org/10.1021/acs.jctc.1c00527.

[55] K. Schütt, O. Unke, and M. Gastegger, "Equivariant message passing for the prediction of tensorial properties and molecular spectra," in *International Conference on Machine Learning* (PMLR, 2021) pp. 9377–9388.

[56] S. Batzner, A. Musaelian, L. Sun, M. Geiger, J. P. Mailoa, M. Kornbluth, N. Molinari, T. E. Smidt, and B. Kozinsky, "E(3)-equivariant graph neural networks for data-efficient and accurate interatomic potentials," Nat. Commun. **13**, 2453 (2022).

[57] M. Haghighatlari, J. Li, X. Guan, O. Zhang, A. Das, C. J. Stein, F. Heidar-Zadeh, M. Liu, M. Head-Gordon, L. Bertels, H. Hao, I. Leven, and T. Head-Gordon, "NewtonNet: a newtonian message passing network for deep learning of interatomic potentials and forces," Digital Discovery **1**, 333–343 (2022).

[58] I. Batatia, D. P. Kovács, G. N. C. Simm, C. Ortner, and G. Csányi, "MACE: Higher order equivariant message passing neural networks for fast and accurate force fields," (2023), arXiv:2206.07697 [stat.ML].

[59] A. Musaelian, S. Batzner, A. Johansson, L. Sun, C. J. Owen, M. Kornbluth, and B. Kozinsky, "Learning local equivariant representations for large-scale atomistic dynamics," Nat. Commun. **14**, 579 (2023).

[60] W. G. Stark, J. Westermayr, O. A. Douglas-Gallardo, J. Gardner, S. Habershon, and R. J. Maurer, "Machine learning interatomic potentials for reactive hydrogen dynamics at metal surfaces based on iterative refinement of reaction probabilities," The Journal of Physical Chemistry C **127**, 24168–24182 (2023), https://doi.org/10.1021/acs.jpcc.3c06648.

[61] Y. Wang, T. Wang, S. Li, X. He, M. Li, Z. Wang, N. Zheng, B. Shao, and T.-Y. Liu, "Enhancing geometric representations for molecules with equivariant vector-scalar interactive message passing," Nature Communications **15**, 313 (2024).

[62] D. P. Kingma and J. Ba, "Adam: A method for stochastic optimization," (2014).

[63] M. Geiger, T. Smidt, M. Alby, B. K. Miller, W. Boomsma, B. Dice, K. Lapchevskyi, M. Weiler, Michał Tyszkiewicz, M. Uhrin, S. Batzner, D. Madisetti, J. Frellsen, N. Jung, S. Sanborn, Jkh, Mingjian Wen, J. Rackers, M. Rød, and M. Bailey, "e3nn/e3nn: 2022-12-12," (2022).

[64] A. Paszke, S. Gross, F. Massa, A. Lerer, J. Bradbury, G. Chanan, T. Killeen, Z. Lin, N. Gimelshein, L. Antiga, A. Desmaison, A. Köpf, E. Yang, Z. DeVito, M. Raison, A. Tejani, S. Chilamkurthy, B. Steiner, L. Fang, J. Bai, and S. Chintala, "PyTorch: An imperative style, high-performance deep learning library," (2019).

[65] J. Hutter, M. Iannuzzi, F. Schiffmann, and J. VandeVondele, "CP2K: atomistic simulations of condensed matter systems," WIREs Computational Molecular Science **4**, 15–25 (2014), https://wires.onlinelibrary.wiley.com/doi/pdf/10.1002/wcms.1159.

[66] P. Pernot, "The long road to calibrated prediction uncertainty in computational chemistry," The Journal of Chemical Physics **156**, 114109 (2022), https://pubs.aip.org/aip/jcp/article-pdf/doi/10.1063/5.0084302/16539431/114109_1_online.pdf.

[67] Y. Hu, J. Musielewicz, Z. W. Ulissi, and A. J. Medford, "Robust and scalable uncertainty estimation with conformal prediction for machine-learned interatomic potentials," Machine Learning: Science and Technology **3**, 045028 (2022).

[68] K. Tran, W. Neiswanger, J. Yoon, Q. Zhang, E. Xing, and Z. W. Ulissi, "Methods for comparing uncertainty quantifications for material property predictions," Machine Learning: Science and Technology **1**, 025006 (2020).

[69] V. Zaverkin, D. Holzmüller, H. Christiansen, F. Errica, F. Alesiani, M. Takamoto, M. Niepert, and J. Kästner, "Uncertainty-biased molecular dynamics for learning uniformly accurate interatomic potentials," npj Computational Materials **10**, 83 (2024).

[70] A. N. Angelopoulos and S. Bates, "A gentle introduction to conformal prediction and distribution-free uncertainty quantification," (2022), arXiv:2107.07511 [cs.LG].

[71] A. P. Thompson, H. M. Aktulga, R. Berger, D. S. Bolintineanu, W. M. Brown, P. S. Crozier, P. J. in 't Veld, A. Kohlmeyer, S. G. Moore, T. D. Nguyen, R. Shan, M. J. Stevens, J. Tranchida, C. Trott, and S. J. Plimpton, "LAMMPS - a flexible simulation tool for particle-based materials modeling at the atomic, meso, and continuum scales," Computer Physics Communications **271**, 108171 (2022).

[72] M. Shuaibi and Z. Ulissi, "AmpTorch: Atomistic machine-learning package - pytorch," `https://github.com/ulissigroup/amptorch` (2023).

[73] M. Brehm, M. Thomas, S. Gehrke, and B. Kirchner, "TRAVIS—A free analyzer for trajectories from molecular simulation," The Journal of Chemical Physics **152**, 164105 (2020), https://pubs.aip.org/aip/jcp/article-pdf/doi/10.1063/5.0005078/16692963/164105_1_online.pdf.

[74] G. J. Martyna, D. J. Tobias, and M. L. Klein, "Constant pressure molecular dynamics algorithms," The Journal of Chemical Physics **101**, 4177–4189 (1994).

[75] J. Wang, R. M. Wolf, J. W. Caldwell, P. A. Kollman, and D. A. Case, "Development and testing of a general AMBER force field," Journal of Computational Chemistry **25**, 1157–1174 (2004), https://onlinelibrary.wiley.com/doi/pdf/10.1002/jcc.20035.

[76] P. Li, L. F. Song, and K. M. J. Merz, "Systematic parameterization of monovalent ions employing the nonbonded model," Journal of Chemical Theory and Computation **11**, 1645–1657 (2015), pMID: 26574374, https://doi.org/10.1021/ct500918t.

[77] A. Jakalian, B. L. Bush, D. B. Jack, and C. I. Bayly, "Fast, efficient generation of high-quality atomic charges. AM1-BCC model: I. method," Journal of Computational Chemistry **21**, 132–146 (2000), https://doi.org/10.1002/(SICI)1096-987X(20000130)21:2<132::AID-JCC5>3.0.CO;2-P.

[78] M. Brehm and B. Kirchner, "TRAVIS - a free analyzer and visualizer for monte carlo and molecular dynamics trajectories," Journal of Chemical Information and Modeling **51**, 2007–2023 (2011), pMID: 21761915, https://doi.org/10.1021/ci200217w.

[79] Y. Hu, Z. Wang, H. Li, X. Huang, and L. Chen, "Spectroscopic and DFT studies to understand the liquid formation mechanism in the LiTFSI/acetamide complex system," Spectrochimica Acta Part A: Molecular and Biomolecular Spectroscopy **61**, 2009–2015 (2005).

[80] O. Shayestehpour and S. Zahn, "Molecular features of reline and homologous deep eutectic solvents contributing to nonideal mixing behavior," The Journal of Physical Chemistry B **124**, 7586–7597 (2020), pMID: 32790398.

[81] Z. Li, G. D. Smith, and D. Bedrov, "Li+ solvation and transport properties in ionic liquid/lithium salt mixtures: A molecular dynamics simulation study," The Journal of Physical Chemistry B **116**, 12801–12809 (2012), pMID: 22978679, https://doi.org/10.1021/jp3052246.

[82] V. Lesch, Z. Li, D. Bedrov, O. Borodin, and A. Heuer, "The influence of cations on lithium ion coordination and transport in ionic liquid electrolytes: a md simulation study," Phys. Chem. Chem. Phys. **18**, 382–392 (2016).

[83] J. Zhang, J. Pagotto, T. Gould, and T. T. Duignan, "Scalable molecular simulation of electrolyte solutions with quantum chemical accuracy," (2024), arXiv:2310.12535 [physics.chem-ph].

[84] K. Fujii, T. Fujimori, T. Takamuku, R. Kanzaki, Y. Umebayashi, and S.-i. Ishiguro, "Conformational equilibrium of bis(trifluoromethanesulfonyl) imide anion of a room-temperature ionic liquid: Raman spectroscopic study and DFT calculations," The Journal of Physical Chemistry B **110**, 8179–8183 (2006), pMID: 16623493, https://doi.org/10.1021/jp0612477.

[85] J.-P. Hansen and I. R. McDonald, "Chapter 10 - ionic liquids," in *Theory of Simple Liquids (Third Edition)*, edited by J.-P. Hansen and I. R. McDonald (Academic Press, Burlington, 2006) third edition ed., pp. 291–340.

[86] J. Smiatek, A. Heuer, and M. Winter, "Properties of ion complexes and their impact on charge transport in organic solvent-based electrolyte solutions for lithium batteries: Insights from a theoretical perspective," Batteries **4** (2018), 10.3390/batteries4040062.

[87] K. M. Diederichsen, E. J. McShane, and B. D. McCloskey, "Promising routes to a high Li+ transference number electrolyte for lithium ion batteries," ACS Energy Letters **2**, 2563–2575 (2017), https://doi.org/10.1021/acsenergylett.7b00792.

[88] K. Shigenobu, S. Tsuzuki, F. Philippi, T. Sudoh, Y. Ugata, K. Dokko, M. Watanabe, K. Ueno, and W. Shinoda, "Molecular level origin of ion dynamics in highly concentrated electrolytes," The Journal of Physical Chemistry B **127**, 10422–10433 (2023), pMID: 38015036, https://doi.org/10.1021/acs.jpcb.3c05864.

[89] C. Rey-Castro and L. F. Vega, "Transport properties of the ionic liquid 1-ethyl-3-methylimidazolium chloride from equilibrium molecular dynamics simulation. the effect of temperature," The Journal of Physical Chemistry B **110**, 14426–14435 (2006), pMID: 16854152.

[90] A. France-Lanord and J. C. Grossman, "Correlations from ion pairing and the Nernst-Einstein equation," Phys. Rev. Lett. **122**, 136001 (2019).

[91] A. Verdaguer, J. A. Padró, and J. Trullàs, "Molecular dynamics study of the velocity cross-correlations in liquids," The Journal of Chemical Physics **109**, 228–234 (1998).